
Maximum Likelihood Training of Autoencoders

Peter Sorrenson*
Computer Vision and Learning Lab
Heidelberg University

Felix Draxler*
Computer Vision and Learning Lab
Heidelberg University

Armand Rousselot
Computer Vision and Learning Lab
Heidelberg University

Sander Hummerich
Computer Vision and Learning Lab
Heidelberg University

Lea Zimmermann
Computer Vision and Learning Lab
Heidelberg University

Ullrich Köthe
Computer Vision and Learning Lab
Heidelberg University

Abstract

Maximum likelihood training has favorable statistical properties and is popular for generative modeling, especially with normalizing flows. On the other hand, generative autoencoders promise to be more efficient than normalizing flows due to the manifold hypothesis. In this work, we introduce successful maximum likelihood training of unconstrained autoencoders for the first time, bringing the two paradigms together. To do so, we identify and overcome two challenges: Firstly, existing maximum likelihood estimators for free-form networks are unacceptably slow, relying on iteration schemes whose cost scales linearly with latent dimension. We introduce an improved estimator which eliminates iteration, resulting in constant cost (roughly double the runtime per batch of a vanilla autoencoder). Secondly, we demonstrate that naively applying maximum likelihood to autoencoders can lead to divergent solutions and use this insight to motivate a stable maximum likelihood training objective. We perform extensive experiments on toy, tabular and image data, demonstrating the competitive performance of the resulting model. We call our model the maximum likelihood autoencoder (MLAE).

1 Introduction

Generative modeling is one of the most important tasks in machine learning, having numerous applications across vision [Rombach et al., 2022], language modeling [Brown et al., 2020], scientific applications [Ardizzone et al., 2018, Radev et al., 2020] and beyond. One of the best-motivated approaches to generative modeling is maximum likelihood training, due to its favorable statistical properties [Hastie et al., 2009]. In the continuous setting, exact maximum likelihood training is most commonly achieved by normalizing flows [Rezende and Mohamed, 2015, Dinh et al., 2014, Kobyzev et al., 2020] which parameterize an exactly invertible function with a tractable change of variables (log-determinant term). This generally introduces a trade-off between model expressivity and computational cost, where the cheapest networks to train and sample from, such as coupling block architectures, require very specifically constructed functions which may limit expressivity [Draxler et al., 2022]. In addition, normalizing flows preserve the dimensionality of the inputs, requiring a latent space of the same dimension as the data space.

*Equal contribution. Correspondence to peter.sorrenson@iwr.uni-heidelberg.de.

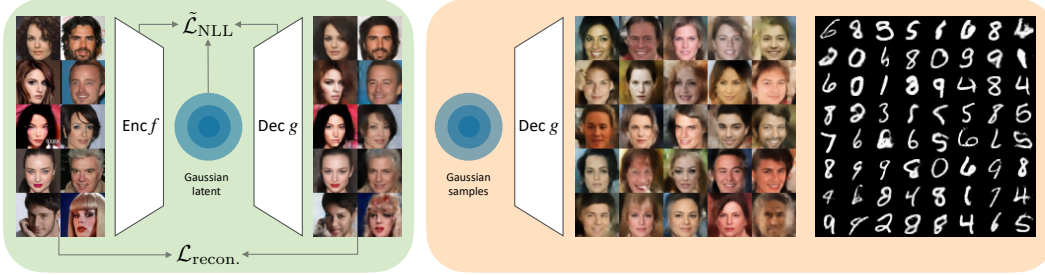


Figure 1: **Maximum likelihood autoencoders (MLAE) training and inference.** (Left) We combine a reconstruction loss $\mathcal{L}_{\text{recon.}}$ with a novel maximum likelihood loss $\tilde{\mathcal{L}}_{\text{NLL}}$ to obtain an autoencoder with a Gaussian latent space. (Right) We generate novel samples by decoding standard normal latent samples with our best-performing models on CelebA and MNIST. The reconstructions shown are on CelebA validation data, the samples are uncurated samples from our models.

Due to the manifold hypothesis [Bengio et al., 2013], which suggests that realistic data lies on a low-dimensional manifold embedded into a high-dimensional data space, it is more efficient to only model distributions on a low-dimensional manifold and regard deviations from the manifold as uninformative noise. A natural tool for learning low-dimensional manifolds is the autoencoder and many attempts have been made to develop generative versions of this architecture, which transform the training data into a simple latent distribution, typically standard normal, via the encoder. Generating from the model is achieved by passing samples from the latent distribution through the decoder (see fig. 1).

Prior works such as Caterini et al. [2021], Brehmer and Cranmer [2020] have used some version of exact maximum likelihood training in combination with autoencoders, though invariably with autoencoder architectures adapted from the normalizing flow literature (known as “invertible autoencoders” [Teng and Choromanska, 2019] or “injective flows” [Kothari et al., 2021]) where encoder and decoder share parameters. The restrictive architectures used in such models were originally introduced for tractable change of variables calculation in normalizing flows, but such calculations are not possible in the presence of a bottleneck [Brehmer and Cranmer, 2020]. As a result, we propose to drop the restrictive constructions (such as coupling blocks) and use an unconstrained encoder and decoder, as in a standard autoencoder. This simplifies the design of the model and makes it more expressive. To our knowledge, we are the first work to introduce exact maximum likelihood training with unconstrained autoencoders.

We build on the unbiased maximum likelihood estimator used in rectangular flows [Caterini et al., 2021]. We simplify it considerably by replacing iterative conjugate gradient, which can require iteration of up to the number of latent dimensions to converge, with a single step estimator. This allows us to train our autoencoder models almost as fast as a vanilla autoencoder. Specifically, our loss function and its gradient can be computed in about twice the time (or less) as the reconstruction loss and its gradient. In addition, we make a novel observation about generative autoencoders: naively training with maximum likelihood is ill-defined due to the possibility of diverging curvature in the decoding function. To fix this problem, we propose a modification to our maximum likelihood estimator which counteracts the possibility of diverging curvature. We call our model the *maximum likelihood autoencoder* (MLAE).

To summarize, we make the following contributions:

- We introduce an efficient exact maximum likelihood estimator for unconstrained autoencoders, making them a practical generative model (section 4.1).
- We identify pathological behavior in the naive application of maximum likelihood training in the presence of a bottleneck, and offer a solution to avoid this behavior while maintaining computational efficiency (section 4.2).
- We demonstrate competitive performance with a series of experiments on toy, tabular and image data (section 5). We provide code to implement our model and reproduce our results at <https://github.com/vislearn/MLAE>.

2 Related work

At the heart of maximum likelihood training lies the need to estimate the Jacobian determinant of the transformation to calculate the change of variables. Efficient computation of this determinant traditionally imposed two major restrictions on normalizing flow architectures: Firstly, the latent space has to match in dimension with the data space. Secondly, normalizing flows are restricted to certain functional forms, such as coupling and autoregressive blocks. Below we outline the existing approaches to overcome these problems and how our solution compares.

Lower-dimensional latent spaces One set of methods attempts to use full-dimensional normalizing flows, with some additional regularization or architectural constraints such that a subspace of the latent space corresponds to the manifold. One strategy adds noise to the data to make it a full-dimensional distribution then denoises to the manifold [Horvat and Pfister, 2021, Loaiza-Ganem et al., 2023]. Another restricts the non-manifold latent dimensions to have small variance [Beitler et al., 2021].

Other methods sidestep the problem by making training into a two-step procedure. First, an autoencoder is trained on reconstruction loss, then a normalizing flow is trained to learn the resulting latent distribution. Brehmer and Cranmer [2020] and Kothari et al. [2021] use an injective flow, while Böhm and Seljak [2020] use unconstrained networks as autoencoder. Ghosh et al. [2019] additionally regularize the decoder.

Conformal embedding flows [Ross and Cresswell, 2021] ensure the decomposition of the determinant into the contribution from each block by exclusively using conformal transformations. However, the resulting transformations are quite restrictive.

The most similar work to ours is the rectangular flow [Caterini et al., 2021] which estimates the gradient of the log-determinant via an iterative, unbiased estimator. The resulting method is quite slow to train, and uses injective flows, which are restrictive.

Unconstrained normalizing flow architectures Several works attempt to reduce the constraints imposed by typical normalizing flow architectures, allowing the use of free-form networks. FFJORD [Grathwohl et al., 2018] is a type of continuous normalizing flow [Chen et al., 2018b] which estimates the change of variables stochastically. Residual flows [Behrmann et al., 2019, Chen et al., 2019] make residual networks invertible, but require expensive iterative estimators to train via maximum likelihood. Self-normalizing flows [Keller et al., 2021] and relative gradient optimization [Gresele et al., 2020] estimate maximum likelihood gradients for the matrices used in neural networks, but restrict the architecture to use exclusively square weight matrices without skip connections.

Approximating maximum likelihood Many methods optimize some bound on the maximum likelihood, notably the variational autoencoder [Kingma and Welling, 2013] and its variants. Cunningham et al. [2020] also optimizes a variational lower bound to the likelihood. Kumar et al. [2020], Zhang et al. [2020] approximate the log-determinant of the Jacobian by its Frobenius norm. The entropic AE [Ghose et al., 2020] maximizes the entropy of the latent distribution by a nearest-neighbor estimator while constraining its variance, resulting in a Gaussian latent space. In addition, there are other ways to regularize the latent space which are not based on maximum likelihood, e.g. adversarial methods [Makhzani et al., 2015].

In contrast to the above, our approach uses exact maximum likelihood with an unconstrained architecture, which easily accommodates a lower-dimensional latent space.

3 Background

Autoencoders Autoencoders are defined by a pair of models, an encoder $f : \mathbb{R}^D \rightarrow \mathbb{R}^d$ which compresses data to a lower-dimensional latent space and a decoder $g : \mathbb{R}^d \rightarrow \mathbb{R}^D$ which decompresses the latent representation. The goal is to learn models such that a reconstructed instance $\hat{x} = g(f(x))$ is close to its original value despite being compressed through a lower-dimensional bottleneck. The closeness is most often measured by the squared Euclidean distance which gives rise to the reconstruction loss:

$$\mathcal{L}_{\text{recon.}} = E_{p_{\text{data}}(x)} [\|\hat{x} - x\|^2]. \tag{1}$$

The image of g , which we will also call the *decoder manifold*, is defined as the set of points $\{g(z) \mid z \in \mathbb{R}^d\}$, which is a d -dimensional manifold embedded in \mathbb{R}^D . The optimal encoder will be such that \hat{x} is an orthogonal projection onto the decoder manifold and the optimal decoder $g(z)$ will output the mean value of all x such that $f(x) = z$. The optimal encoder and decoder form a pseudoinverse pair, defined below.

Pseudoinverse pair We call f and g a *pseudoinverse pair* if $f \circ g$ is the identity. Equivalently, $g \circ f$ is a *projection*: a reconstructed sample $\hat{x} = g(f(x))$ does not change on further application of $g \circ f$, i.e. $(g \circ f) \circ (g \circ f) = (g \circ f)$. We call f a pseudoinverse of g and g a pseudoinverse of f if f and g form a pseudoinverse pair. Note that if $d < D$ a pseudoinverse pair is not unique for a given f or g : the only requirement on f is that it inverts g on its image; its behavior elsewhere is unconstrained. Equally, the only requirement on g is that it maps to some point in its preimage, so $g(z) = x$ for some x such that $f(x) = z$, but which point is not specified. We can remove these degrees of freedom by requiring that f and g minimize the reconstruction loss, having the properties given in the previous paragraph.

Change of variables across dimensions Normalizing flow models, trained by maximum likelihood via the change of variables theorem, are only defined when mapping between spaces of equal dimension. A result from differential geometry [Krantz and Parks, 2008] allows us to generalize the change of variables theorem to non-equal-dimension transformations through the formula:

$$p_X(x) = p_Z(f(x)) \left(\det [g'(f(x))^\top g'(f(x))] \right)^{-\frac{1}{2}}, \quad (2)$$

where f and g are a pseudoinverse pair and primes denote derivatives: $g'(f(x))$ is the Jacobian matrix of g evaluated at $f(x)$. Note that, since p_X is derived as the pushforward of the latent distribution p_Z by g , the formula is valid only for x which lie on the decoder manifold (see appendix A for more details).

Injective flows Injective flows, also called invertible autoencoders [Teng and Choromanska, 2019, Brehmer and Cranmer, 2020], parameterize f and g as the composition of two invertible functions, w defined in \mathbb{R}^D and h defined in \mathbb{R}^d , with a slicing/padding operation in between:

$$f = h^{-1} \circ \text{slice} \circ w^{-1} \quad \text{and} \quad g = w \circ \text{pad} \circ h, \quad (3)$$

where $\text{slice}(x)$ selects the first d elements of x and $\text{pad}(z)$ concatenates $D - d$ zeros to the end of z . Since slice and pad are a pseudoinverse pair, so too are f and g .

Rectangular flows Minimizing the negative logarithm of eq. (2) and adding a Lagrange multiplier to restrict the distance of data points from the decoder manifold results in the following per-sample loss term:

$$\mathcal{L}_{\text{RF}}(x) = -\log p_Z(z) + \frac{1}{2} \log \det [g'(z)^\top g'(z)] + \beta \|\hat{x} - x\|^2, \quad (4)$$

where $z = f(x)$ and β is a hyperparameter.

The log-determinant term is the difficult one to optimize. Fortunately, its gradient with respect to the parameters θ of the decoder can be estimated tractably [Caterini et al., 2021]. Note that $g = g_\theta$ but the θ subscript is dropped to avoid clutter. The relevant quantity is (with $J = g'(z)$):

$$\frac{\partial}{\partial \theta_j} \frac{1}{2} \log \det (J^\top J) = \frac{1}{2} \text{tr} \left((J^\top J)^{-1} \frac{\partial}{\partial \theta_j} (J^\top J) \right). \quad (5)$$

The trace can be estimated with a trace estimator [Hutchinson, 1989, Girard, 1989]:

$$\frac{\partial}{\partial \theta_j} \frac{1}{2} \log \det (J^\top J) \approx \frac{1}{2K} \sum_{k=1}^K \epsilon_k^\top (J^\top J)^{-1} \frac{\partial}{\partial \theta_j} (J^\top J) \epsilon_k, \quad (6)$$

where the ϵ_k are sampled from a distribution where $E[\epsilon \epsilon^\top] = \mathbb{I}$, typically either Rademacher or standard normal. Matrix multiplication can be avoided by using vector-matrix and matrix-vector product subroutines. These are readily obtained by automatic differentiation in the case of vector products with $J^\top J$ and by autodiff combined with the conjugate gradient iterative method for $(J^\top J)^{-1}$ products. Write $\epsilon_k^\top (J^\top J)^{-1} = \text{CG}(J^\top J; \epsilon_k)^\top$ where $\text{CG}(A; b)$ denotes the solution to

$Ax = b$ via conjugate gradient. The parameter derivative can be made to act only on the rightmost Jacobian terms by applying the stop-gradient operation, to the output of the conjugate gradient method. The final surrogate loss function for the log-determinant term is therefore:

$$\frac{1}{2K} \sum_{k=1}^K \text{stop_gradient} \left(\text{CG} \left(J^\top J; \epsilon_k \right)^\top \right) J^\top J \epsilon_k, \quad (7)$$

which replaces the log-determinant term in the loss. The function `stop_gradient` returns its input, but makes it constant with respect to parameters. Note that the resulting loss does not have the same value as, but shares the gradient with the original loss in eq. (4).

4 Maximum likelihood autoencoder (MLAE)

Our modification to rectangular flows is threefold: first, we use an unconstrained autoencoder architecture (no restrictively parameterized invertible functions); second, we introduce a more computationally efficient surrogate estimator; third, we modify the surrogate to avoid pathological behavior related to manifolds with high curvature. Our per-sample loss function is:

$$\mathcal{L}(x) = -\log p_Z(z) - \frac{1}{K} \sum_{k=1}^K \epsilon_k^\top f'(x) \text{stop_gradient} (g'(z) \epsilon_k) + \beta \|\hat{x} - x\|^2, \quad (8)$$

with $z = f(x)$. Note the negative sign before the surrogate term, which comes from sending the log-determinant gradient to the encoder rather than the decoder. We will derive and motivate this formulation of the loss in sections 4.1 to 4.2.

4.1 Simplifying the surrogate

We considerably simplify the optimization of rectangular flows by a new surrogate for the log-determinant term, which uses the Jacobian of the encoder as an approximation for the inverse Jacobian of the decoder. This allows the surrogate to be computed in a single pass, avoiding costly conjugate gradient iterations.

We do this by expanding the derivative in eq. (5):

$$\frac{1}{2} \text{tr} \left((J^\top J)^{-1} \frac{\partial}{\partial \theta_j} (J^\top J) \right) = \text{tr} \left(J^\dagger \frac{\partial}{\partial \theta_j} J \right), \quad (9)$$

where $J^\dagger = (J^\top J)^{-1} J^\top$ is the pseudoinverse of J . The full derivation is in appendix B. To see the advantage of this formulation consider that for a pseudoinverse pair f and g :

$$\frac{\partial}{\partial z} f(g(z)) = f'(g(z)) g'(z) = \mathbb{I}, \quad (10)$$

since $f \circ g$ is the identity function. By substituting $f(x)$ for z , we see that the pseudoinverse of the Jacobian of g evaluated at $f(x)$ is just the Jacobian of f evaluated at \hat{x} . Using the `stop_gradient` operation, this leads to the following surrogate loss term:

$$\frac{1}{K} \sum_{k=1}^K \text{stop_gradient} \left(\epsilon_k^\top f'(\hat{x}) \right) g'(z) \epsilon_k, \quad (11)$$

or equivalently, using the encoder Jacobian in place of the decoder Jacobian (see appendix B):

$$-\frac{1}{K} \sum_{k=1}^K \epsilon_k^\top f'(\hat{x}) \text{stop_gradient} (g'(z) \epsilon_k). \quad (12)$$

Each term of the sum can be computed from just two vector-Jacobian products obtained from backward-mode automatic differentiation. This is a significant improvement on the iterative conjugate gradient method needed in the original formulation of rectangular flows which requires up to $2(d+1)$ vector-Jacobian or Jacobian-vector products to ensure convergence [Caterini et al., 2021]. We measure $\sim 1.5 \times$ to $2 \times$ the wall clock time of our loss compared to reconstruction loss only, independent of the latent dimension. Note that the surrogate is only accurate if f is (at least approximately) a pseudoinverse for g . We assume that this is sufficiently fulfilled in our model due to the presence of the reconstruction loss and we observe stable training in practice, thus validating the assumption.

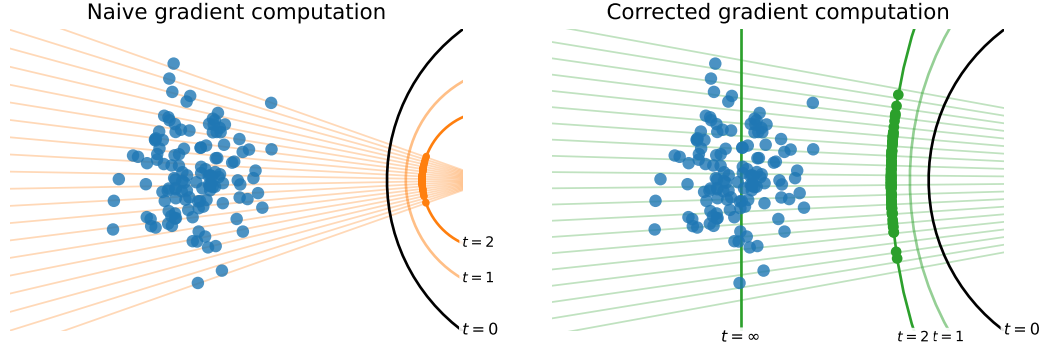


Figure 2: Naive training of autoencoders with negative log-likelihood (NLL, see section 4.2) leads to pathological solutions (*left*). Starting with the initialization ($t = 0$, black), gradient steps increase the curvature of the learnt manifold ($t = 1, 2$, orange). This reduces NLL because the entropy of the projected data is reduced, by moving the points closer to one another. This effect is stronger than the reconstruction loss. We fix this problem by evaluating the volume change off-manifold (*right*). This moves the manifold closer to the data and reduces the curvature ($t = 1, 2$, green), until it eventually centers the manifold on the data with zero curvature ($t = \infty$, green). Light lines show the set of points which map to the same latent point. Data is projected onto the $t = 2$ manifold.

4.2 Problems with maximum likelihood in the presence of a bottleneck

Rectangular flows are trained with a combination of a reconstruction and likelihood term. We might ask what happens if we only train with the likelihood term, making an analogy to normalizing flows. In this case our loss would be:

$$\mathcal{L}_{\text{NLL}}(x) = -\log p_Z(z) + \frac{1}{2} \log \det [g'(z)^\top g'(z)]. \quad (13)$$

Unfortunately, optimizing this loss can lead us to learn a degenerate decoder manifold, an issue raised in Brehmer and Cranmer [2020]. Here we expand on their argument to show why the model will tend to learn a manifold which aligns with the lowest entropy directions of the data. We show how to fix this problem in the linear case with the addition of a reconstruction term but show that adding a reconstruction term in the nonlinear case is not sufficient to avoid pathological solutions.

First consider that the per-sample loss is invariant to projections: $\mathcal{L}_{\text{NLL}}(\hat{x}) = \mathcal{L}_{\text{NLL}}(x)$, since $\mathcal{L}_{\text{NLL}}(x)$ is a function only of $f(x)$ and $f(\hat{x}) = f(x)$. This means that we can write our loss as:

$$\mathcal{L}_{\text{NLL}} = E_{p_{\text{data}}(x)}[\mathcal{L}_{\text{NLL}}(x)] = E_{\hat{p}_{\text{data}}(\hat{x})}[\mathcal{L}_{\text{NLL}}(\hat{x})], \quad (14)$$

where $\hat{p}_{\text{data}}(\hat{x})$ is the probability density of the projection of the training data onto the decoder manifold. Now consider that the negative log-likelihood loss is one part of a KL divergence, and KL divergences are always non-negative:

$$KL(\hat{p}_{\text{data}}(\hat{x}) || p_\theta(\hat{x})) = -H(\hat{p}_{\text{data}}(\hat{x})) - E_{p_{\text{data}}(\hat{x})}[\log p_\theta(\hat{x})] \geq 0. \quad (15)$$

As a result, the loss is lower bounded by the entropy of the data projected onto the manifold:

$$\mathcal{L}_{\text{NLL}} = -E_{\hat{p}_{\text{data}}(\hat{x})}[\log p_\theta(\hat{x})] \geq H(\hat{p}_{\text{data}}(\hat{x})). \quad (16)$$

Unlike in standard normalizing flow optimization, where the right hand side would be fixed, giving the loss a well-defined lower bound, in this case the entropy on the right depends on the learned model, and the loss can continue to decrease without bound by reducing the entropy of the projected data. See fig. 2 (*left*) for an illustration of a pathological case. This is a toy model with a 1-dimensional latent space where the decoder maps to a semicircle with learnable radius which is offset horizontally. The encoder projects orthogonally onto the manifold. Naively optimizing the likelihood leads to increasing curvature since this decreases the entropy of the projected data indefinitely.

Since it is clear that optimization of a likelihood loss without reconstruction will fail, we ask what happens as we reintroduce a reconstruction loss at various strengths. Suppose the loss is of the form:

$$\mathcal{L} = \mathcal{L}_{\text{NLL}} + \beta E_{p_{\text{data}}(x)}[\|\hat{x} - x\|^2]. \quad (17)$$

In appendix C the closed-form solution to this model is worked out in detail when f and g are linear functions. The model learns low-entropy directions of the data when β is too low but transitions to the PCA solution for large enough β . This transition occurs at $\beta = 1/2\sigma^2$ where σ is the smallest eigenvalue of the data covariance matrix.

Unfortunately, when f and g are non-linear, the addition of a reconstruction term is not enough to fix the pathological behavior of the likelihood loss defined on the manifold. Consider again fig. 2, where the left-hand figure is optimized with both likelihood and reconstruction loss. Without additional constraints on the decoding function, the curvature can increase without bound, leading to a loss tending towards negative infinity.

Towards a well-behaved loss The term which leads to pathological behavior in the likelihood loss is the log-determinant. In the original formulation, this expression is evaluated after projecting x to the manifold. We make the fairly simple modification of evaluating f' at x rather than \hat{x} . Namely, we modify eq. (12) to estimate the gradient of the log-determinant term by:

$$-\frac{1}{K} \sum_{k=1}^K \epsilon_k^\top f'(x) \text{stop_gradient}(g'(z)\epsilon_k). \quad (18)$$

Using the change of variables with f' evaluated at \hat{x} , on the manifold, all that matters is the change of volume from the projected data to the latent space, so we can decrease $-\log \det(f'(\hat{x})f'(\hat{x})^\top)$ (and hence the loss) by choosing a manifold which concentrates the projected data more tightly. Concentration effects due to curvature happen when data is on the concave side of the manifold (as in fig. 2). In this setting, a perturbation to x will not change the resulting $f(x)$ very much, an effect that becomes stronger with more curvature. As a result, $f'(x)$ becomes smaller as curvature increases. This increases the loss and thus counteracts the undesired concentration effect. In this way, we discourage pathological solutions involving high curvature. In fig. 2 (*right*) we can see the effect of the modified estimator: the manifold now moves towards the data since the optimization is not dominated by diverging curvature.

Along with the results of section 4.1, this leads to the following loss (same as eq. (8)):

$$\begin{aligned} \mathcal{L}(x) &= \tilde{\mathcal{L}}_{\text{NLL}}(x) + \beta \mathcal{L}_{\text{recon.}}(x) \\ &= -\log p_Z(z) - \frac{1}{K} \sum_{k=1}^K \epsilon_k^\top f'(x) \text{stop_gradient}(g'(z)\epsilon_k) + \beta \|\hat{x} - x\|^2. \end{aligned} \quad (19) \quad (20)$$

Note that we could have modified eq. (11) (replacing \hat{x} with x) instead of modifying eq. (12), but we found that giving gradient from the log-determinant term to the encoder led to more stable training.

5 Experiments

In this section, we demonstrate the empirical success of the proposed model. First, we analyze the influence of the reconstruction weight on model behavior. Second, we compare our model to rectangular flows on tabular data. Finally, we show competitive performance on the Pythae image generation benchmark Chadebec et al. [2022], achieving the best FID score in some categories.

Code to implement the model and to reproduce our results is provided at <https://github.com/vislearn/MLAE>.

5.1 Characterization of model behavior

Implementation details In implementing the trace estimator, we have to make a number of choices. Briefly, i) we chose to formulate the log-determinant gradient in terms of the encoder rather than decoder as it was more stable in practice, ii) we performed traces in the order $f'(x)g'(z)$ as this reduces variance, iii) we used a mixture of forward- and backward-mode autograd as this was compatible with our estimator, and iv) we used orthogonalized Gaussian noise in the trace estimator. Full justification for these choices is given in appendix D.

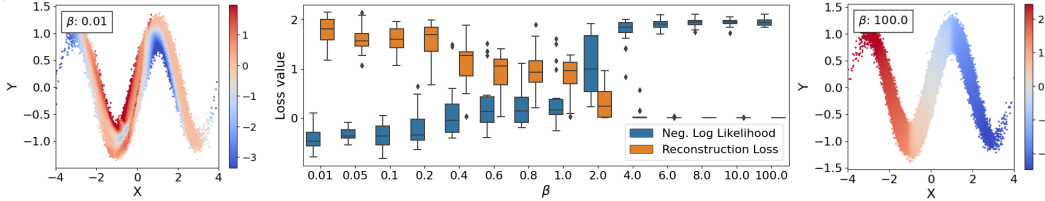


Figure 3: Learning a noisy 2-D sinusoid with a 1-D latent space for different reconstruction weights β . Color codes denote the value of the latent variable at each location. When the reconstruction term has low weight (*left*), the autoencoder learns to throw away information about the position along the sinusoid and only retains the orthogonal noise. Only sufficiently high weights (*right*) result in the desired solution, where the decoder spans the sinusoid manifold. The middle plot shows the tradeoff between reconstruction error and NLL as we transition between these regimes (box plots indicate variability across runs).

Table 1: Comparison of performance on FID-like (lower is better) metric between rectangular flows and our method on tabular datasets [Papamakarios et al., 2017].

Method	POWER	GAS	HEPMASS	MINIBOONE
Rectangular Flows ($K = 1$)	0.083 \pm 0.015	0.110 \pm 0.021	0.779 \pm 0.191	1.001 \pm 0.051
MLAE (<i>ours</i>) ($K = 1$)	0.109 \pm 0.052	0.377 \pm 0.038	0.710 \pm 0.020	0.772 \pm 0.034

Toy data To further illustrate the problems of maximum likelihood training in the presence of a bottleneck, we consider a 2-D sinusoid subjected to Gaussian noise (fig. 3). The autoencoder should converge to a manifold that spans the sinusoid. However, this only happens when the reconstruction weight β in the loss eq. (8) is sufficiently high (fig. 3 right). Otherwise, our analysis in section 4.2 predicts that the loss is minimized by a projection with minimal entropy. In other words, the latent codes for small β represent the direction *orthogonal* to the manifold, and the autoencoder learns the noise instead of the sinusoid (fig. 3 left). We demonstrate in appendix E.1 that the point at which β becomes sufficiently large varies between datasets.

Conditional MNIST We train models on MNIST, conditioned on the digit labels, across different reconstruction weights and analyze how well each model reconstructs the data manifold. We measure this by the entropy of the learned distribution and the visual diversity of the generated samples, which both increase with reconstruction weight, as expected. We find that the convergence towards a Gaussian latent distribution slows down for very large reconstruction weights, as the gradient is then dominated by the reconstruction loss, see appendix E.2.

5.2 Model benchmarking

Tabular Data We evaluate our method on four of the tabular datasets used by Papamakarios et al. [2017], using the same data splits, and make a comparison to the published rectangular flow results [Caterini et al., 2021], see table 1. We adopt the “FID-like metric” from that work, which computes the Wasserstein-2 distance between the closest Gaussian distributions to the test data and to the data generated by the model. This is a measure of the difference of the means and covariance matrices of the generated and test datasets. We note that the results are comparable, with our method underperforming on GAS but achieving a better result on MINIBOONE. However we emphasize the greatly reduced runtime of our method: while the rectangular flow experiments were trained for around 1-2 hours per run, our runs each took under 10 minutes. Full experimental and runtime details are in appendix E.3.

Image generation on Pythae benchmark We test our approach in the Pythae benchmark for generating images with autoencoders [Chadebec et al., 2022]. We train the architectures they propose using our loss from section 4.2. For selecting hyperparameters, we follow the instructions from the benchmark by selecting the best model by validation FID from 10 different configurations: We test

Table 2: **Benchmark results on CelebA**, following Chadebec et al. [2022]. We train their architectures (ConvNet and ResNet) with our new training objective, achieving SOTA FID on ResNet. We draw latent samples from standard normal “ \mathcal{N} ” or a GMM fit using training data “GMM”. Models with multiple variants (indicated in brackets) have been merged to indicate only the best result across variants. We mark the best FID in each column in bold and underline the second best. As the benchmark chooses the best of 10 models to report, no standard deviations are provided.

Model	ConvNet + \mathcal{N}		ResNet + \mathcal{N}		ConvNet + GMM		ResNet + GMM	
	FID ↓	IS ↑	FID	IS	FID	IS	FID	IS
VAE [Kingma and Welling, 2013]	54.8	1.9	66.6	1.6	52.4	1.9	63.0	1.7
IWAE [Burda et al., 2015]	55.7	1.9	67.6	1.6	52.7	1.9	64.1	1.7
VAE-lin NF [Rezende and Mohamed, 2015]	56.5	1.9	67.1	1.6	53.3	1.9	62.8	1.7
VAE-IAF [Kingma et al., 2016]	55.4	1.9	66.2	1.6	53.6	1.9	62.7	1.7
β -(TC) VAE [Higgins et al., 2017, Chen et al., 2018a]	55.7	1.8	65.9	1.6	51.7	1.9	59.3	1.7
FactorVAE [Kim and Mnih, 2018]	53.8	1.9	66.4	1.7	52.4	2.0	63.3	1.7
InfoVAE - (RBF/IMQ) [Zhao et al., 2017]	55.5	1.9	66.4	1.6	52.7	1.9	62.3	1.7
AAE [Makhzani et al., 2015]	59.9	1.8	64.8	1.7	53.9	2.0	58.7	1.8
MSSSIM-VAE [Snell et al., 2017]	124.3	1.3	119.0	1.3	124.3	1.3	119.2	1.3
VAEGAN [Larsen et al., 2016]	39.7	1.9	122.8	2.0	35.6	1.8	84.3	1.7
Vanilla AE	327.7	1.0	275.0	2.9	55.4	2.0	<u>57.4</u>	1.8
WAE - (RBF/IMQ) [Tolstikhin et al., 2017]	64.6	1.7	67.1	1.6	51.7	2.0	57.7	1.8
VQVAE [Van Den Oord et al., 2017]	306.9	1.0	140.3	2.2	51.6	2.0	57.9	1.8
RAE - (L2/GP) Ghosh et al. [2019]	86.1	2.8	168.7	3.1	52.5	1.9	58.3	1.8
MLAE (ours)	56.9	2.1	62.3	1.7	<u>47.3</u>	1.9	55.0	1.8
MLAE (ours, modified architecture)	47.6	1.7	-	-	39.7	2.0	-	-

different reconstruction weights $\beta = 5, 10, 15, 20, 25$, and number of Hutchinson samples $K = 1, 2$. We give details on the training procedure in appendix E.4.

The Pythae benchmark trains on images from MNIST [LeCun et al., 2010] (data $D = 784$, latent $d = 16$), CIFAR10 [Krizhevsky, 2009] ($D = 3072$, $d = 256$), and CelebA [Liu et al., 2015] ($D = 12288$, $d = 64$). To get latent samples, Pythae proposes to sample from a standard normal, and a GMM with 10 components fit to the training latent codes.

We report Inception Score (IS) [Salimans et al., 2016] and Fréchet Inception Distance (FID) [Heusel et al., 2017] on CelebA in table 2. We achieve SOTA on the ResNet architecture, and perform competitively on the ConvNet architecture. We point to appendix E.4 for detailed results on CelebA, MNIST and CIFAR10.

We notice that we can further improve performance via a small but important change to the architecture: The architectures in Pythae consist of several convolutional layers, followed by a single fully-connected layer which projects to the latent dimension. Adding more fully-connected layers, we can further improve our FID score to 47.6 with the normal sampler, and 39.7 with the GMM sampler (see table 2 and fig. 1 for samples). This only adds 2% additional parameters compared to the Pythae ConvNet. On MNIST, we find that a network with only 1/5th of the number of parameters of the corresponding Pythae model reduces the FID by a factor of 1/2 for the normal sampler. We argue that the inductive bias from a mainly convolutional network prevents having latent dimensions that are independent from one another as their receptive field is limited.

Due to the high computational cost of running the 570 new benchmark models that would result from adding a new architecture to Pythae (requiring several hundreds to thousand GPU hours), we leave a full re-run of this optimization for future work.

Based on the impact of minor changes to the model architecture, we believe that the full potential of our model stands to be realized.

6 Conclusions

This paper offers a computationally efficient solution to maximum likelihood training on manifolds, which we call the maximum-likelihood autoencoder (MLAE). We significantly improve an existing estimator, note that it can be applied to unconstrained autoencoders, analyze problems with naive maximum-likelihood training and offer a solution, and implement and test our model on toy, tabular and image datasets. We find that the model is practical and scalable, showing similar or better performance to other autoencoder generative models on a benchmark. As our work is concerned with

improving generative models, we do not foresee any direct negative societal consequences resulting from our work, though note that it is possible to misuse generative models.

Several theoretical and practical questions remain for future work. We motivate our improved loss (section 4.2) heuristically, but are unsure what objective the gradient corresponds to. Fitting a GMM to the latent space after training improves performance, suggesting that our latent distributions are not perfectly Gaussian. We speculate that this could be due to the encoder and decoder not being a true pseudoinverse pair, or is a consequence of manifold overfitting [Loaiza-Ganem et al., 2022], or could be due to the inductive bias of the benchmark architecture and leave potential theoretical or practical improvements to future work.

7 Acknowledgements

This work is supported by Deutsche Forschungsgemeinschaft (DFG, German Research Foundation) under Germany’s Excellence Strategy EXC-2181/1 - 390900948 (the Heidelberg STRUCTURES Cluster of Excellence). AR acknowledges funding from the Carl-Zeiss-Stiftung. LZ acknowledges support by the German Federal Ministry of Education and Research (BMBF) (project EMUNE/031L0293A). We thank the Center for Information Services and High Performance Computing (ZIH) at TU Dresden for its facilities for high throughput calculations. The authors acknowledge support by the state of Baden-Württemberg through bwHPC and the German Research Foundation (DFG) through grant INST 35/1597-1 FUGG.

References

- Martín Abadi, Ashish Agarwal, Paul Barham, Eugene Brevdo, Zhifeng Chen, Craig Citro, Greg S. Corrado, Andy Davis, Jeffrey Dean, Matthieu Devin, Sanjay Ghemawat, Ian Goodfellow, Andrew Harp, Geoffrey Irving, Michael Isard, Yangqing Jia, Rafal Jozefowicz, Lukasz Kaiser, Manjunath Kudlur, Josh Levenberg, Dandelion Mané, Rajat Monga, Sherry Moore, Derek Murray, Chris Olah, Mike Schuster, Jonathon Shlens, Benoit Steiner, Ilya Sutskever, Kunal Talwar, Paul Tucker, Vincent Vanhoucke, Vijay Vasudevan, Fernanda Viégas, Oriol Vinyals, Pete Warden, Martin Wattenberg, Martin Wicke, Yuan Yu, and Xiaoqiang Zheng. TensorFlow: Large-scale machine learning on heterogeneous systems, 2015. URL <https://www.tensorflow.org/>. Software available from [tensorflow.org](https://www.tensorflow.org/).
- Lynton Ardizzone, Jakob Kruse, Sebastian Wirkert, Daniel Rahner, Eric W Pellegrini, Ralf S Klessen, Lena Maier-Hein, Carsten Rother, and Ullrich Köthe. Analyzing inverse problems with invertible neural networks. *arXiv preprint arXiv:1808.04730*, 2018.
- Jens Behrmann, Will Grathwohl, Ricky TQ Chen, David Duvenaud, and Jörn-Henrik Jacobsen. Invertible residual networks. In *International Conference on Machine Learning*, pages 573–582. PMLR, 2019.
- Jan Jetze Beitler, Ivan Sosnovik, and Arnold Smeulders. Pie: Pseudo-invertible encoder. *arXiv:2111.00619*, 2021.
- Yoshua Bengio, Aaron Courville, and Pascal Vincent. Representation learning: A review and new perspectives. *IEEE transactions on pattern analysis and machine intelligence*, 35(8):1798–1828, 2013.
- Vanessa Böhm and Uroš Seljak. Probabilistic auto-encoder. *arXiv:2006.05479*, 2020.
- Johann Brehmer and Kyle Cranmer. Flows for simultaneous manifold learning and density estimation. *Advances in Neural Information Processing Systems*, 33:442–453, 2020.
- Tom Brown, Benjamin Mann, Nick Ryder, Melanie Subbiah, Jared D Kaplan, Prafulla Dhariwal, Arvind Neelakantan, Pranav Shyam, Girish Sastry, Amanda Askell, et al. Language models are few-shot learners. *Advances in neural information processing systems*, 33:1877–1901, 2020.
- Yuri Burda, Roger Grosse, and Ruslan Salakhutdinov. Importance weighted autoencoders. *arXiv preprint arXiv:1509.00519*, 2015.

- Anthony L Caterini, Gabriel Loaiza-Ganem, Geoff Pleiss, and John P Cunningham. Rectangular flows for manifold learning. *Advances in Neural Information Processing Systems*, 34:30228–30241, 2021.
- Clément Chadebec, Louis J. Vincent, and Stéphanie Allasonnière. Pythae: Unifying Generative Autoencoders in Python – A Benchmarking Use Case. In S. Koyejo, S. Mohamed, A. Agarwal, D. Belgrave, K. Cho, and A. Oh, editors, *Advances in Neural Information Processing Systems* 35, pages 21575–21589. Curran Associates, Inc., 2022. URL <https://arxiv.org/abs/2206.08309>.
- Ricky TQ Chen, Xuechen Li, Roger B Grosse, and David K Duvenaud. Isolating sources of disentanglement in variational autoencoders. *Advances in neural information processing systems*, 31, 2018a.
- Ricky TQ Chen, Yulia Rubanova, Jesse Bettencourt, and David K Duvenaud. Neural ordinary differential equations. *Advances in neural information processing systems*, 31, 2018b.
- Ricky TQ Chen, Jens Behrmann, David K Duvenaud, and Jörn-Henrik Jacobsen. Residual flows for invertible generative modeling. *Advances in Neural Information Processing Systems*, 32, 2019.
- Edmond Cunningham, Renos Zabounidis, Abhinav Agrawal, Madalina Fiterau, and Daniel Sheldon. Normalizing flows across dimensions. *arXiv:2006.13070*, 2020.
- Laurent Dinh, David Krueger, and Yoshua Bengio. Nice: Non-linear independent components estimation. *arXiv preprint arXiv:1410.8516*, 2014.
- Felix Draxler, Christoph Schnoerr, and Ullrich Koethe. Whitening convergence rate of coupling-based normalizing flows. In *Advances in Neural Information Processing Systems*, 2022.
- William Falcon and The PyTorch Lightning team. PyTorch Lightning, March 2019. URL <https://github.com/Lightning-AI/lightning>.
- Amur Ghose, Abdullah Rashwan, and Pascal Poupart. Batch norm with entropic regularization turns deterministic autoencoders into generative models. In *Conference on Uncertainty in Artificial Intelligence*, pages 1079–1088. PMLR, 2020.
- Partha Ghosh, Mehdi SM Sajjadi, Antonio Vergari, Michael Black, and Bernhard Schölkopf. From variational to deterministic autoencoders. *arXiv:1903.12436*, 2019.
- A Girard. A fast ‘Monte-Carlo cross-validation’ procedure for large least squares problems with noisy data. *Numerische Mathematik*, 56:1–23, 1989.
- Gene H Golub and Victor Pereyra. The differentiation of pseudo-inverses and nonlinear least squares problems whose variables separate. *SIAM Journal on numerical analysis*, 10(2):413–432, 1973.
- Will Grathwohl, Ricky TQ Chen, Jesse Bettencourt, Ilya Sutskever, and David Duvenaud. Ffjord: Free-form continuous dynamics for scalable reversible generative models. *arXiv:1810.01367*, 2018.
- Luigi Gresele, Giancarlo Fissore, Adrián Javaloy, Bernhard Schölkopf, and Aapo Hyvarinen. Relative gradient optimization of the jacobian term in unsupervised deep learning. *Advances in neural information processing systems*, 33:16567–16578, 2020.
- Charles R. Harris, K. Jarrod Millman, Stéfan J. van der Walt, Ralf Gommers, Pauli Virtanen, David Cournapeau, Eric Wieser, Julian Taylor, Sebastian Berg, Nathaniel J. Smith, Robert Kern, Matti Picus, Stephan Hoyer, Marten H. van Kerkwijk, Matthew Brett, Allan Haldane, Jaime Fernández del Río, Mark Wiebe, Pearu Peterson, Pierre Gérard-Marchant, Kevin Sheppard, Tyler Reddy, Warren Weckesser, Hameer Abbasi, Christoph Gohlke, and Travis E. Oliphant. Array programming with NumPy. *Nature*, 585(7825):357–362, September 2020. doi: 10.1038/s41586-020-2649-2. URL <https://doi.org/10.1038/s41586-020-2649-2>.
- Trevor Hastie, Robert Tibshirani, and Jerome H Friedman. *The elements of statistical learning: data mining, inference, and prediction*, volume 2. Springer, 2009.

- Martin Heusel, Hubert Ramsauer, Thomas Unterthiner, Bernhard Nessler, and Sepp Hochreiter. Gans trained by a two time-scale update rule converge to a local nash equilibrium. *Advances in neural information processing systems*, 30, 2017.
- Irina Higgins, Loic Matthey, Arka Pal, Christopher Burgess, Xavier Glorot, Matthew Botvinick, Shakir Mohamed, and Alexander Lerchner. beta-vae: Learning basic visual concepts with a constrained variational framework. In *International conference on learning representations*, 2017.
- Christian Horvat and Jean-Pascal Pfister. Denoising normalizing flow. *Advances in Neural Information Processing Systems*, 34:9099–9111, 2021.
- J. D. Hunter. Matplotlib: A 2d graphics environment. *Computing in Science & Engineering*, 9(3): 90–95, 2007. doi: 10.1109/MCSE.2007.55.
- Michael F Hutchinson. A stochastic estimator of the trace of the influence matrix for Laplacian smoothing splines. *Communications in Statistics-Simulation and Computation*, 18(3):1059–1076, 1989.
- Thomas A Keller, Jorn WT Peters, Priyank Jaini, Emiel Hooeboom, Patrick Forré, and Max Welling. Self normalizing flows. In *International Conference on Machine Learning*, pages 5378–5387. PMLR, 2021.
- Hyunjik Kim and Andriy Mnih. Disentangling by factorising. In *International Conference on Machine Learning*, pages 2649–2658. PMLR, 2018.
- Diederik P Kingma and Max Welling. Auto-encoding variational bayes. *arXiv:1312.6114*, 2013.
- Durk P Kingma, Tim Salimans, Rafal Jozefowicz, Xi Chen, Ilya Sutskever, and Max Welling. Improved variational inference with inverse autoregressive flow. *Advances in neural information processing systems*, 29, 2016.
- Ivan Kobyzev, Simon JD Prince, and Marcus A Brubaker. Normalizing flows: An introduction and review of current methods. *IEEE transactions on pattern analysis and machine intelligence*, 43(11):3964–3979, 2020.
- Konik Kothari, AmirEhsan Khorashadizadeh, Maarten de Hoop, and Ivan Dokmanić. Trumpets: Injective flows for inference and inverse problems. In *Uncertainty in Artificial Intelligence*, pages 1269–1278. PMLR, 2021.
- Steven G Krantz and Harold R Parks. *Geometric integration theory*. Springer Science & Business Media, 2008.
- Alex Krizhevsky. Learning multiple layers of features from tiny images. Technical report, 2009.
- Abhishek Kumar, Ben Poole, and Kevin Murphy. Regularized autoencoders via relaxed injective probability flow. In *International Conference on Artificial Intelligence and Statistics*, pages 4292–4301. PMLR, 2020.
- Anders Boesen Lindbo Larsen, Søren Kaae Sønderby, Hugo Larochelle, and Ole Winther. Autoencoding beyond pixels using a learned similarity metric. In *International conference on machine learning*, pages 1558–1566, 2016.
- Yann LeCun, Corinna Cortes, and CJ Burges. Mnist handwritten digit database. *ATT Labs [Online]*. Available: <http://yann.lecun.com/exdb/mnist>, 2, 2010.
- Ziwei Liu, Ping Luo, Xiaogang Wang, and Xiaoou Tang. Deep learning face attributes in the wild. In *ICCV*, pages 3730–3738. IEEE Computer Society, 2015. ISBN 978-1-4673-8391-2. URL <http://dblp.uni-trier.de/db/conf/iccv/iccv2015.html#LiuLWT15>.
- Gabriel Loaiza-Ganem, Brendan Leigh Ross, Jesse C Cresswell, and Anthony L Caterini. Diagnosing and fixing manifold overfitting in deep generative models. *arXiv preprint arXiv:2204.07172*, 2022.
- Gabriel Loaiza-Ganem, Brendan Leigh Ross, Luhuan Wu, John Patrick Cunningham, Jesse C Cresswell, and Anthony L Caterini. Denoising deep generative models. In *Proceedings on*, pages 41–50. PMLR, 2023.

- Alireza Makhzani, Jonathon Shlens, Navdeep Jaitly, Ian Goodfellow, and Brendan Frey. Adversarial autoencoders. *arXiv:1511.05644*, 2015.
- Francesco Mezzadri. How to generate random matrices from the classical compact groups. *arXiv preprint math-ph/0609050*, 2006.
- The pandas development team. pandas-dev/pandas: Pandas, February 2020. URL <https://doi.org/10.5281/zenodo.3509134>.
- George Papamakarios, Theo Pavlakou, and Iain Murray. Masked autoregressive flow for density estimation. *Advances in neural information processing systems*, 30, 2017.
- Adam Paszke, Sam Gross, Francisco Massa, Adam Lerer, James Bradbury, Gregory Chanan, Trevor Killeen, Zeming Lin, Natalia Gimelshein, Luca Antiga, et al. Pytorch: An imperative style, high-performance deep learning library. *Advances in neural information processing systems*, 32, 2019.
- Stefan T Radev, Ulf K Mertens, Andreas Voss, Lynton Ardizzone, and Ullrich Köthe. Bayesflow: Learning complex stochastic models with invertible neural networks. *IEEE transactions on neural networks and learning systems*, 33(4):1452–1466, 2020.
- Danilo Rezende and Shakir Mohamed. Variational inference with normalizing flows. In *International conference on machine learning*, pages 1530–1538. PMLR, 2015.
- Robin Rombach, Andreas Blattmann, Dominik Lorenz, Patrick Esser, and Björn Ommer. High-resolution image synthesis with latent diffusion models. In *Proceedings of the IEEE/CVF Conference on Computer Vision and Pattern Recognition*, pages 10684–10695, 2022.
- Brendan Ross and Jesse Cresswell. Tractable density estimation on learned manifolds with conformal embedding flows. *Advances in Neural Information Processing Systems*, 34:26635–26648, 2021.
- Tim Salimans, Ian Goodfellow, Wojciech Zaremba, Vicki Cheung, Alec Radford, and Xi Chen. Improved techniques for training gans. *Advances in neural information processing systems*, 29, 2016.
- Jake Snell, Karl Ridgeway, Renjie Liao, Brett D Roads, Michael C Mozer, and Richard S Zemel. Learning to generate images with perceptual similarity metrics. In *2017 IEEE International Conference on Image Processing (ICIP)*, pages 4277–4281. IEEE, 2017.
- Yunfei Teng and Anna Choromanska. Invertible autoencoder for domain adaptation. *Computation*, 7(2):20, 2019.
- Ilya Tolstikhin, Olivier Bousquet, Sylvain Gelly, and Bernhard Schoelkopf. Wasserstein auto-encoders. *arXiv:1711.01558*, 2017.
- Aaron Van Den Oord, Oriol Vinyals, et al. Neural discrete representation learning. *Advances in neural information processing systems*, 30, 2017.
- Wes McKinney. Data Structures for Statistical Computing in Python. In Stéfan van der Walt and Jarrod Millman, editors, *Proceedings of the 9th Python in Science Conference*, pages 56 – 61, 2010. doi: 10.25080/Majora-92bf1922-00a.
- Zijun Zhang, Ruixiang Zhang, Zongpeng Li, Yoshua Bengio, and Liam Paull. Perceptual generative autoencoders. In *International Conference on Machine Learning*, pages 11298–11306, 2020.
- Shengjia Zhao, Jiaming Song, and Stefano Ermon. Infovae: Information maximizing variational autoencoders. *arXiv:1706.02262*, 2017.

A Change of variables formula across dimensions

The change of variables formula describes how probability densities change as they are mapped through an injective “pushforward” function g . It is instructive to derive this formula when g is an invertible function. Let p_Z be a base density and p_X the pushforward density obtained by mapping samples from p_Z through g . Then we can write

$$p_X(x) = \int p(x | z)p_Z(z)dz \quad (21)$$

$$= \int \delta(x - g(z))p_Z(z)dz \quad (22)$$

$$= \int \delta(x - \hat{x})p_Z(f(\hat{x})) |\det(g'(f(\hat{x})))|^{-1} d\hat{x} \quad (23)$$

$$= p_Z(f(x)) |\det(g'(f(\hat{x})))|^{-1} \quad (24)$$

using the change of variables $\hat{x} = g(z)$, meaning that $z = f(\hat{x})$ and $|\det(g'(z))|dz = d\hat{x}$ with f the inverse of g .

Now suppose that g maps from \mathbb{R}^d to \mathbb{R}^D with $d < D$. We can generalize the change of variables $\hat{x} = g(z)$ using $z = f(\hat{x})$ and $\det(g'(z)^\top g'(z))^\frac{1}{2} dz = d\hat{x}$ where f is a pseudoinverse for g (see chapter 5 of Krantz and Parks [2008]). This gives us

$$p_X(x) = \int \delta(x - g(z))p_Z(z)dz \quad (25)$$

$$= \int \delta(x - \hat{x})p_Z(f(\hat{x})) \det(g'(f(\hat{x}))^\top g'(f(\hat{x})))^{-\frac{1}{2}} d\hat{x} \quad (26)$$

This expression defines a probability density in the full ambient space \mathbb{R}^D but we cannot easily remove the integral. However, we can convert it into an expression resembling the full-dimensional case, but defined only on the image of g :

$$p_X(x) = p_Z(f(x)) \det(g'(f(x))^\top g'(f(x)))^{-\frac{1}{2}} \quad (27)$$

Note that this expression only integrates to 1 if we restrict integration to the image of g . As such, it should only be regarded as defining a probability distribution on this manifold, not in the ambient space \mathbb{R}^D .

B Derivation of gradient estimator

We expand the derivative in eq. (5):

$$\frac{\partial}{\partial \theta_j} \frac{1}{2} \log \det J^\top J = \frac{1}{2} \text{tr} \left((J^\top J)^{-1} \frac{\partial}{\partial \theta_j} (J^\top J) \right) \quad (28)$$

$$= \frac{1}{2} \text{tr} \left((J^\top J)^{-1} \left(\frac{\partial}{\partial \theta_j} J^\top \right) J \right) + \frac{1}{2} \text{tr} \left((J^\top J)^{-1} J^\top \left(\frac{\partial}{\partial \theta_j} J \right) \right) \quad (29)$$

$$= \frac{1}{2} \text{tr} \left((J(J^\top J)^{-1})^\top \frac{\partial}{\partial \theta_j} J \right) + \frac{1}{2} \text{tr} \left((J^\top J)^{-1} J^\top \frac{\partial}{\partial \theta_j} J \right) \quad (30)$$

$$= \text{tr} \left((J^\top J)^{-1} J^\top \frac{\partial}{\partial \theta_j} J \right) \quad (31)$$

$$= \text{tr} \left(J^\dagger \frac{\partial}{\partial \theta_j} J \right) \quad (32)$$

where we used the cyclic property of the trace and that $\text{tr}(AB) = \text{tr}(A^\top B^\top)$. $J^\dagger = (J^\top J)^{-1} J^\top$ is the matrix pseudoinverse of J .

Now we will do an equivalent derivation for the encoder. Observe that, since

$$(J^\dagger J^{\dagger\top})^{-1} = ((J^\top J)^{-1} J^\top J (J^\top J)^{-1})^{-1} = J^\top J \quad (33)$$

we can rewrite the log-determinant term using the encoder Jacobian:

$$\frac{1}{2} \log \det(J^\top J) = -\frac{1}{2} \log \det(J^\dagger J^{\dagger\top}) \quad (34)$$

Note the negative sign on the right-hand side.

The derivation for the derivative is very similar to that for the decoder, where we now take a derivative with respect to encoder parameters ϕ :

$$\frac{\partial}{\partial \phi_j} \frac{1}{2} \log \det J^\dagger J^{\dagger\top} = \frac{1}{2} \operatorname{tr} \left((J^\dagger J^{\dagger\top})^{-1} \frac{\partial}{\partial \phi_j} (J^\dagger J^{\dagger\top}) \right) \quad (35)$$

$$= \frac{1}{2} \operatorname{tr} \left((J^\dagger J^{\dagger\top})^{-1} \left(\frac{\partial}{\partial \phi_j} J^\dagger \right) J^{\dagger\top} \right) + \frac{1}{2} \operatorname{tr} \left((J^\dagger J^{\dagger\top})^{-1} J^\dagger \left(\frac{\partial}{\partial \phi_j} J^{\dagger\top} \right) \right) \quad (36)$$

$$= \frac{1}{2} \operatorname{tr} \left(J^{\dagger\top} (J^\dagger J^{\dagger\top})^{-1} \frac{\partial}{\partial \phi_j} J^\dagger \right) + \frac{1}{2} \operatorname{tr} \left(((J^\dagger J^{\dagger\top})^{-1} J^\dagger)^\top \frac{\partial}{\partial \phi_j} J^{\dagger\top} \right) \quad (37)$$

$$= \operatorname{tr} \left(J^{\dagger\top} (J^\dagger J^{\dagger\top})^{-1} \frac{\partial}{\partial \phi_j} J^\dagger \right) \quad (38)$$

$$= \operatorname{tr} \left(J \frac{\partial}{\partial \phi_j} J^\dagger \right) \quad (39)$$

where we used the cyclic property of the trace, that $\operatorname{tr}(AB) = \operatorname{tr}(A^\top B^\top)$ and that $J = (J^\dagger)^\dagger = J^{\dagger\top} (J^\dagger J^{\dagger\top})^{-1}$.

Recall eq. (11) in section 4.1, which gives the surrogate for the log-determinant term:

$$\frac{1}{K} \sum_{k=1}^K \operatorname{stop_gradient} (\epsilon_k^\top f'(\hat{x})) g'(z) \epsilon_k, \quad (40)$$

This is formulated in terms of the Jacobian of the decoder, in other words it is derived from $\det(J^\top J)$. The equivalent term, formulated in terms of the Jacobian of the encoder should be derived from $\det(J^\dagger J^{\dagger\top})$ and is therefore (note the negative sign):

$$-\frac{1}{K} \sum_{k=1}^K \epsilon_k^\top f'(\hat{x}) \operatorname{stop_gradient} (g'(z) \epsilon_k) \quad (41)$$

We write it in the order $f'(\hat{x})g'(z)$ rather than $g'(z)f'(\hat{x})$ since this reduces the variance of the estimate. See appendix D.1 for further details.

C Linear model trained on maximum likelihood alone

Consider a linear model, trained on data with zero mean and covariance Σ . Let the encoder function be $f(x) = Ax$ and suppose that A has positive singular values, meaning that AA^\top is positive definite. Let the decoder function be $g(z) = A^\dagger z$, where $A^\dagger = A^\top (AA^\top)^{-1}$. We want to minimize a combination of negative log-likelihood and a reconstruction loss:

$$\mathcal{L} = \mathcal{L}_{\text{NLL}} + \mathcal{L}_{\text{recon.}} \quad (42)$$

$$= E_x \left[\frac{1}{2} \|Ax\|^2 - \frac{1}{2} \log \det(AA^\top) + \frac{1}{2\sigma^2} \|A^\dagger Ax - x\|^2 \right] \quad (43)$$

$$= \frac{1}{2} E_x [x^\top A^\top Ax] - \frac{1}{2} \log \det(AA^\top) + \frac{1}{2\sigma^2} E_x [x^\top (A^\dagger A - \mathbb{I})^2 x] \quad (44)$$

$$= \frac{1}{2} \operatorname{tr}(A E_x [xx^\top] A^\top) - \frac{1}{2} \log \det(AA^\top) + \frac{1}{2\sigma^2} \operatorname{tr}(E_x [xx^\top] (\mathbb{I} - A^\dagger A)) \quad (45)$$

$$= \frac{1}{2} \operatorname{tr}(A \Sigma A^\top) - \frac{1}{2} \log \det(AA^\top) + \frac{1}{2\sigma^2} \operatorname{tr}(\Sigma (\mathbb{I} - A^\dagger A)) \quad (46)$$

where A is a full rank $d \times D$ matrix with $d \leq D$.

Before solving for the minimum, let's review some matrix calculus identities. It is often convenient to consider A as a function of a single variable x , differentiate with respect to x , and then choose x to be A_{ij} . Then the derivative is

$$\frac{d}{dA_{ij}}A = E^{(ij)} \quad (47)$$

where $E^{(ij)}$ is a matrix of zeros, except for the ij entry which is a one. We can write this as $E_{kl}^{(ij)} = \delta_{ik}\delta_{jl}$ where δ is the Kronecker delta. When evaluating $E^{(ij)}$ inside a trace we get the simple expression:

$$\text{tr}(E^{(ij)}B) = E_{kl}^{(ij)}B_{lk} = \delta_{ik}\delta_{jk}B_{lk} = B_{ji} \quad (48)$$

using Einstein notation. The additional matrix identities we will need are Jacobi's formula for a square invertible matrix B :

$$\frac{d}{dx} \det(B) = \det(B) \text{tr} \left(B^{-1} \left(\frac{d}{dx} B \right) \right) \quad (49)$$

and hence

$$\frac{d}{dx} \log \det(B) = \text{tr} \left(B^{-1} \left(\frac{d}{dx} B \right) \right) \quad (50)$$

and we will prove the following lemma.

Lemma C.1. *Suppose the matrix A depends on a variable x . Then we have the following expression for the derivative of the projection operator $A^\dagger A$:*

$$\frac{d}{dx}(A^\dagger A) = A^\dagger \left(\frac{d}{dx} A \right) (\mathbb{I} - A^\dagger A) + \left(A^\dagger \left(\frac{d}{dx} A \right) (\mathbb{I} - A^\dagger A) \right)^\top \quad (51)$$

Proof. The following is based on the proof to lemma 4.1 in Golub and Pereyra [1973]. Define the projection operator $P_A = A^\dagger A$ and its complement $P_A^\perp = \mathbb{I} - P_A$. Then, since $P_A P_A = P_A$,

$$\left(\frac{d}{dx} P_A \right) = \left(\frac{d}{dx} P_A P_A \right) = \left(\frac{d}{dx} P_A \right) P_A + P_A \left(\frac{d}{dx} P_A \right) \quad (52)$$

In addition, since $P_A A^\top = A^\top$

$$\left(\frac{d}{dx} P_A A^\top \right) = \left(\frac{d}{dx} P_A \right) A^\top + P_A \left(\frac{d}{dx} A \right)^\top = \left(\frac{d}{dx} A \right)^\top \quad (53)$$

and therefore

$$\left(\frac{d}{dx} P_A \right) P_A = \left(\frac{d}{dx} P_A \right) A^\top A^{\dagger\top} = \left(\frac{d}{dx} A \right)^\top A^{\dagger\top} - P_A \left(\frac{d}{dx} A \right)^\top A^{\dagger\top} = P_A^\perp \left(\frac{d}{dx} A \right)^\top A^{\dagger\top} \quad (54)$$

By similar steps but using $AP_A = A$, we can derive

$$P_A \left(\frac{d}{dx} P_A \right) = A^\dagger \left(\frac{d}{dx} A \right) P_A^\perp \quad (55)$$

Putting it all together gives

$$\left(\frac{d}{dx} P_A \right) = A^\dagger \left(\frac{d}{dx} A \right) P_A^\perp + \left(A^\dagger \left(\frac{d}{dx} A \right) P_A^\perp \right)^\top \quad (56)$$

Note that the second term is just the transpose of the first. \square

Now we are ready to find the derivative of the loss and set it to zero.

Lemma C.2. *The derivative of the loss with respect to A takes the form:*

$$\frac{d}{dA} \mathcal{L} = \left(\Sigma A^\top - A^\dagger - \frac{1}{\sigma^2} (\mathbb{I} - A^\dagger A) \Sigma A^\dagger \right)^\top \quad (57)$$

Proof. Let's apply the above identities to the first term in the loss:

$$\frac{d}{dx} \frac{1}{2} \text{tr}(A \Sigma A^\top) = \frac{1}{2} \text{tr} \left(\left(\frac{d}{dx} A \right) \Sigma A^\top + A \Sigma \left(\frac{d}{dx} A \right)^\top \right) \quad (58)$$

$$= \text{tr} \left(\left(\frac{d}{dx} A \right) \Sigma A^\top \right) \quad (59)$$

since the trace is invariant under transposition and hence

$$\frac{d}{dA_{ij}} \frac{1}{2} \text{tr}(A \Sigma A^\top) = \text{tr}(E^{(ij)} \Sigma A^\top) = (\Sigma A^\top)_{ji} \quad (60)$$

Applying Jacobi's formula to the second term in the loss gives:

$$\frac{d}{dx} \frac{1}{2} \log \det(AA^\top) = \frac{1}{2} \text{tr} \left((AA^\top)^{-1} \left(\frac{d}{dx} (AA^\top) \right) \right) \quad (61)$$

$$= \frac{1}{2} \text{tr} \left((AA^\top)^{-1} \left(\left(\frac{d}{dx} A \right) A^\top + A \left(\frac{d}{dx} A \right)^\top \right) \right) \quad (62)$$

and therefore

$$\frac{d}{dA_{ij}} \frac{1}{2} \log \det(AA^\top) = \frac{1}{2} \text{tr} \left((AA^\top)^{-1} \left(E^{(ij)} A^\top + A E^{(ji)} \right) \right) \quad (63)$$

$$= \frac{1}{2} \text{tr} \left(E^{(ij)} A^\top (AA^\top)^{-1} + E^{(ij)} A^\top (AA^\top)^{-1} \right) \quad (64)$$

$$= (A^\top (AA^\top)^{-1})_{ji} \quad (65)$$

$$= A_{ji}^\dagger \quad (66)$$

where we used the cyclic and transpose properties of the trace and that $E^{(ji)^\top} = E^{(ij)}$.

The final term requires a derivative of $\text{tr}(\Sigma(\mathbb{I} - A^\dagger A))$, which is equal to a derivative of $-\text{tr}(\Sigma A^\dagger A)$. We use the formula for the derivative of the projection operator to get

$$\frac{d}{dx} \frac{1}{2} \text{tr}(\Sigma A^\dagger A) = \frac{1}{2} \text{tr} \left(\Sigma \left(\frac{d}{dx} (A^\dagger A) \right) \right) \quad (67)$$

$$= \text{tr} \left(\Sigma A^\dagger \left(\frac{d}{dx} A \right) (\mathbb{I} - A^\dagger A) \right) \quad (68)$$

again using the transpose property of the trace, and therefore

$$\frac{d}{dA_{ij}} \frac{1}{2} \text{tr}(\Sigma A^\dagger A) = \text{tr}(E^{(ij)} (\mathbb{I} - A^\dagger A) \Sigma A^\dagger) = ((\mathbb{I} - A^\dagger A) \Sigma A^\dagger)_{ji} \quad (69)$$

Putting the three expressions together, we have that

$$\frac{d}{dA} \mathcal{L} = \left(\Sigma A^\top - A^\dagger - \frac{1}{\sigma^2} (\mathbb{I} - A^\dagger A) \Sigma A^\dagger \right)^\top \quad (70)$$

□

Lemma C.3. *The critical points of \mathcal{L} satisfy the following properties:*

1. $A = U \Sigma^{-\frac{1}{2}}$ with $U U^\top = \mathbb{I}$
2. $U^\top U$ commutes with Σ

Proof. Using lemma C.2, the critical points satisfy

$$\Sigma A^\top - A^\dagger - \frac{1}{\sigma^2} (\mathbb{I} - A^\dagger A) \Sigma A^\dagger = 0 \quad (71)$$

By multiplying by A from the left we have

$$A\Sigma A^\top = \mathbb{I}_d \quad (72)$$

meaning that $U = A\Sigma^{\frac{1}{2}}$ must have orthonormal rows (since $UU^\top = \mathbb{I}$). With this definition, we can write $A = U\Sigma^{-\frac{1}{2}}$.

If we now multiply by A from the right, we get

$$\Sigma A^\top A - A^\dagger A - \frac{1}{\sigma^2} \Sigma A^\dagger A + \frac{1}{\sigma^2} A^\dagger A \Sigma A^\dagger A = 0 \quad (73)$$

Noting that the second and fourth terms are symmetric (since $A^\dagger A$ is symmetric), this means that the remaining terms must be symmetric:

$$\Sigma A^\top A - \frac{1}{\sigma^2} \Sigma A^\dagger A = A^\top A \Sigma - \frac{1}{\sigma^2} A^\dagger A \Sigma \quad (74)$$

Since $A^\top A$ commutes with $A^\dagger A$, they are simultaneously diagonalizable, and since they are both symmetric, they share an orthonormal basis of eigenvectors. Clearly $A^\top A - A^\dagger A/\sigma^2$ has the same basis. Since this matrix commutes with Σ , it must share a basis with Σ and hence Σ has the same basis as $A^\top A$. This means that Σ commutes with $A^\top A$.

Expanding A in terms of U , this means that

$$\Sigma A^\top A = \Sigma^{\frac{1}{2}} U^\top U \Sigma^{-\frac{1}{2}} = \Sigma^{-\frac{1}{2}} U^\top U \Sigma^{\frac{1}{2}} = A^\top A \Sigma \quad (75)$$

and therefore $\Sigma U^\top U = U^\top U \Sigma$, meaning that Σ and $U^\top U$ commute. \square

Consider as an example the case where Σ is diagonal. $U^\top U$ is a projection matrix and in this case must be diagonal due to commuting with Σ . As a result, it must have exactly d ones and $D - d$ zeros along the diagonal. This means that the rows of U are a basis for the d dimensional axis-aligned subspace corresponding to the d nonzero entries. In the case of a non-diagonal Σ , this generalizes to the rows of U spanning the same subspace as some subset of d eigenvectors of Σ . This leads to the expression of the loss function in the next theorem.

Theorem C.4. *Let Σ have the eigen-decomposition $V\Lambda V^\top$ with $\Lambda = \text{diag}(\lambda)$. Let $U^\top U$ have the eigen-decomposition VEV^\top , with $E = \text{diag}(\alpha)$. Then the minimum of the loss is satisfied by α such that*

$$\mathcal{L}_\alpha = \sum_{i=1}^D \frac{1}{2} \alpha_i \left(\log \lambda_i - \frac{1}{\sigma^2} \lambda_i \right) \quad (76)$$

is minimal, subject to the constraint $\alpha_i \in \{0, 1\}$ with $\sum_{i=1}^D \alpha_i = d$.

Proof. Let's note a couple of properties. First, we have $(U\Sigma U^\top)^k = U\Sigma^k U^\top$ due to Σ commuting with $U^\top U$, so we can say that $f(U\Sigma U^\top) = Uf(\Sigma)U^\top$ for any matrix function f with a Taylor series. Next, $U^\top U$ is an orthogonal projection matrix, so E is a diagonal matrix with ones or zeros on the diagonal. We know that the rank of U is d , hence E has exactly d ones and $D - d$ zeros along the diagonal. Therefore we have the constraint $\alpha_i \in \{0, 1\}$ with $\sum_{i=1}^D \alpha_i = d$. Next, note that $A^\dagger A = U^\top U$.

Now we substitute back into the loss in terms of U :

$$\mathcal{L} = \frac{1}{2} \text{tr}(UU^\top) - \frac{1}{2} \log \det(U\Sigma^{-1}U^\top) + \frac{1}{2\sigma^2} \text{tr}(\Sigma(\mathbb{I} - U^\top U)) \quad (77)$$

$$= \frac{1}{2} \text{tr}(U \log(\Sigma) U^\top) - \frac{1}{2\sigma^2} \text{tr}(U\Sigma U^\top) + \text{const.} \quad (78)$$

where we used that

$$\log \det(U\Sigma^{-1}U^\top) = \text{tr} \log(U\Sigma^{-1}U^\top) = -\text{tr}(U \log(\Sigma) U^\top) \quad (79)$$

Note that $\text{tr}(UU^\top)$ is constant. Consider that

$$\text{tr}(U\Sigma U^\top) = \text{tr}(U^\top U \Sigma U^\top U) = \text{tr}(VEDEV^\top) = \text{tr}(EDE) = \alpha \cdot \lambda \quad (80)$$

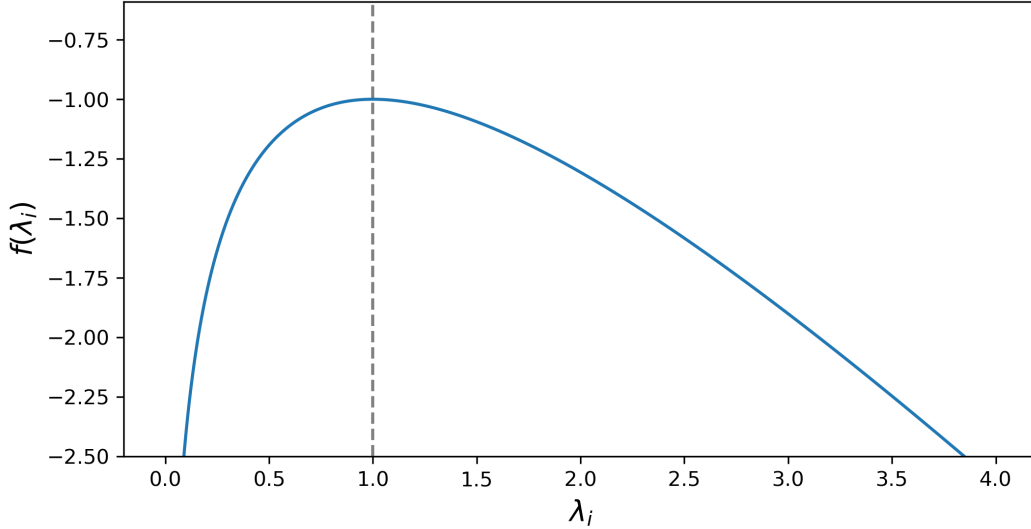


Figure 4: Plot of $f(\lambda_i) = \log \lambda_i - \lambda_i/\sigma^2$ with $\sigma = 1$, showing maximum value at $\lambda_i = \sigma^2$ and unbounded behavior on either side.

The same logic holds for the term with $\log(\Sigma)$. Therefore, dropping constant terms, the loss can be written in terms of α and λ :

$$\mathcal{L}_\alpha = \sum_{i=1}^D \frac{1}{2} \alpha_i \left(\log \lambda_i - \frac{1}{\sigma^2} \lambda_i \right) \quad (81)$$

□

The loss will take different values depending on which elements of α are nonzero. Define $f(\lambda_i) = \log \lambda_i - \lambda_i/\sigma^2$. The loss will be minimized when the nonzero α_i correspond to those values of $f(\lambda_i)$ which are minimal. Clearly $f''(\lambda_i) < 0$, so f has only one maximum at $\lambda_i = \sigma^2$ and is unbounded below on either side of this maximum (see fig. 4). Consider the two extreme cases:

1. All eigenvalues λ are smaller than σ^2 . The minimal values of $f(\lambda_i)$ will occur for the smallest values of λ_i . Hence the d smallest eigenvalues of Σ will be selected.
2. All eigenvalues λ are larger than σ^2 . The minimal values of $f(\lambda_i)$ will occur for the largest values of λ_i . Hence the d largest eigenvalues of Σ will be selected.

In the intermediate regime, there will be a phase transition between these two extremes.

In the first case, the reconstructed manifold will be a projection onto the d -dimensional subspace with the lowest variance, exactly the opposite result to PCA. In the second case, the reconstructed manifold will be a projection onto the d -dimensional subspace with the highest variance, exactly the same result as PCA. If we maximize the likelihood on the manifold without any reconstruction loss, corresponding to the $\sigma^2 \rightarrow \infty$ limit, we actually learn the lowest entropy manifold. It makes more sense to learn the highest entropy manifold as in PCA. We can ensure this is the case by adding Gaussian noise of variance σ^2 to the data, ensuring that the minimum eigenvalue of the covariance matrix is at least σ^2 , even if the original data is degenerate.

D Implementation Details

In implementing the trace estimator, we have to make a number of choices, each elaborated below. The main reasons for each choice are given first, with more technical details deferred to later in the appendix.

Table 3: Different possible estimators for the gradient of the log-determinant term.

	gradient to encoder	gradient to decoder
trace in data space	$-\text{tr} \left(g'(z) \left(\frac{\partial}{\partial \phi_j} f'(x) \right) \right)$	$\text{tr} \left(\left(\frac{\partial}{\partial \theta_j} g'(x) \right) f'(x) \right)$
trace in latent space	$-\text{tr} \left(\left(\frac{\partial}{\partial \phi_j} f'(x) \right) g'(z) \right)$	$\text{tr} \left(f'(x) \left(\frac{\partial}{\partial \theta_j} g'(z) \right) \right)$

Gradient to encoder or decoder The log-determinant term can be formulated either in terms of the Jacobian of the encoder (see eq. (12)) or the decoder (see eq. (11)). As discussed in section 4.2 we find that formulating it in terms of the encoder Jacobian leads to more stable training. Since the training also minimizes the squared norm of $f(x)$, we speculate that having gradient from this term and the log-determinant term both being sent to the encoder allows the encoder to more efficiently shape the latent space distribution. We note the similarity of this formulation to the standard change-of-variables loss used to train normalizing flows. If we instead send the gradient of the log-determinant to the decoder, the information about how the encoder can change can only reach it via the reconstruction term, which doesn't allow the encoder to deviate significantly from being the pseudoinverse of the decoder. A change in the decoder will therefore lead to a corresponding change in the encoder, but this is a less direct process than sending gradient to the encoder directly. In addition, this formulation means the decoder is optimized only to minimize reconstruction loss, meaning that it will likely be an approximate pseudoinverse for the encoder, a condition we require for the accuracy of the surrogate estimator.

Space in which trace is performed Considering eqs. (32) and (39), the central component of the surrogate is a trace (estimator). Making use of the cyclic property of the trace, i.e. $\text{tr}(A^\top B) = \text{tr}(BA^\top)$ for any $A, B \in \mathbb{R}^{D \times d}$, we can choose which expansion of the trace to estimate:

$$\sum_{i=1}^d (A^\top B)_{ii} = \text{tr}(A^\top B) = \text{tr}(BA^\top) = \sum_{i=1}^D (BA^\top)_{ii}. \quad (82)$$

The variance of a stochastic trace estimator depends on the noise used but in general is roughly proportional to the squared Frobenius norm of the matrix (see appendix D.3). Given two matrices $A, B \in \mathbb{R}^{D \times d}$ with $d < D$, it is likely that $\|A^\top B\|_F^2 < \|BA^\top\|_F^2$. This statement is not true for all A and B , but is almost always fulfilled when $d \ll D$.

Transferred to our context: In general the matrices $f'(x) \in \mathbb{R}^{d \times D}$ and $g'(z) \in \mathbb{R}^{D \times d}$ are rectangular and can be multiplied together in either the $f'(x)g'(z) \in \mathbb{R}^{d \times d}$ order or $g'(z)f'(x) \in \mathbb{R}^{D \times D}$ order. This matters for applying the trace since generally $d < D$.

A more precise statement (proven in appendix D.1) is that if the entries of A and B are sampled from standard normal distributions, then $E[\|A^\top B\|_F^2] = Dd^2$ versus $E[\|BA^\top\|_F^2] = D^2d$. For $d \ll D$ the difference becomes significant. The difference between the two estimators may not be large if the two matrices have special structure, in particular if they share a basis. However, since the terms being multiplied in our case are a Jacobian matrix and the derivative of another Jacobian matrix with respect to a parameter θ_j or ϕ_j , it is unlikely that any such particular structure is present.

As a result, when the latent space is smaller than the data space, the preferable estimator is the one that performs the trace in the latent space, meaning that products in the estimator have the order $f'(x)g'(z)$ (see table 3). In appendix D.1.1, we experimentally test the convergence of trace estimators with increasing Hutchinson samples, performed in both data and latent space, confirming that convergence is much faster when performing the trace in latent space.

Type of gradient Consider the estimator:

$$\text{tr} \left(\left(\frac{\partial}{\partial \phi_j} f'(x) \right) g'(z) \right) = \frac{\partial}{\partial \phi_j} E_\epsilon \left[\epsilon^\top f'(x) \text{stop_gradient}(g'(z)) \epsilon \right] \quad (83)$$

Ignoring the stop gradient operation for now, this requires computing terms of the form $\epsilon^\top f'(x)g'(z)\epsilon$. In order to avoid calculating full Jacobian matrices, we can implement the calculation using some

combination of vector-Jacobian (vjp) or Jacobian-vector (jvp) products, which are efficient to compute with backward-mode respectively forward-mode automatic differentiation. Note that we can use the result from one product as the vector for another vjp or jvp. For example, $v_1 := (\epsilon^\top f'(x))^\top \in \mathbb{R}^D$ yields a vector, so we can compute $\epsilon^\top f'(x)g'(z)\epsilon = v_1^\top g'(z)\epsilon$ via two vector-Jacobian products.

This gives us three choices: i) backward mode only (two vjp), ii) forward mode only (two jvp) or iii) a mix of both (one jvp and one vjp). We opt to use mixed mode (see appendix D.2 for further details).

Trace estimator noise Trace estimators rely on the identity $E_\epsilon[\epsilon^\top A \epsilon] = \text{tr}(A E_\epsilon[\epsilon \epsilon^\top]) = \text{tr}(A)$, meaning that we require only $E_\epsilon[\epsilon \epsilon^\top] = \mathbb{I}$ for the noise variable. The choice comes down mainly to the variance of the estimator. Among all noise vectors whose entries are sampled independently, Rademacher noise has the lowest variance [Hutchinson, 1989]. However, if the entries are sampled from a standard normal distribution and then scaled to have length \sqrt{d} where d is the dimension of ϵ , the entries are no longer independent and the variance of the estimator is comparable to Rademacher noise [Girard, 1989]. When using a single Hutchinson sample, we choose to use scaled Gaussian noise for its low variance, and since it covers more directions than Rademacher noise (covering the hypersphere uniformly, rather than at a fixed 2^d points). When we have more than one Hutchinson sample, we additionally orthogonalize the vectors as this further reduces variance. More details are in appendix D.3.

Number of noise samples We can choose to use between 1 and d noise samples in the trace estimator (with d samples we already can calculate the exact trace, so more samples are not necessary). Denote the number of samples by K . We find that in general $K = 1$ is enough for good performance, especially if the batch size is sufficiently high.

D.1 Variance of trace estimator

Theorem D.1. *Let $A, B \in \mathbb{R}^{D \times d}$ where the entries of both matrices are sampled from a standard normal distribution. Then*

$$E[\|A^\top B\|_F^2] = d^2 D \quad \text{and} \quad E[\|BA^\top\|_F^2] = dD^2 \quad (84)$$

Proof. Consider first $\|A^\top B\|_F^2$. We can write this as

$$\|A^\top B\|_F^2 = \sum_{i=1}^d \sum_{j=1}^d \left(\sum_{k=1}^D A_{ki} B_{kj} \right)^2 = \sum_{i,j}^d \sum_{k,l}^D A_{ki} A_{li} B_{kj} B_{lj} \quad (85)$$

Taking an expectation over this expression, the only nonzero contributions will be from terms where the A and B terms are both quadratic, since if not, the term will be multiplied by $E[X] = 0$ where X is standard normal. This requires $k = l$, giving

$$E[\|A^\top B\|_F^2] = \sum_{i,j}^d \sum_k^D E[A_{ki}^2 B_{kj}^2] \quad (86)$$

$$= \sum_{i,j}^d \sum_k^D E[A_{ki}^2] E[B_{kj}^2] \quad (87)$$

$$= d^2 D \quad (88)$$

since A_{ki} and B_{kj} are independent and the expectation of the square of a standard normal variable is its variance, i.e. 1. The equivalent expressions for $\|BA^\top\|_F^2$ can be obtained by swapping d and D in these expressions. \square

D.1.1 Experimental confirmation

To evaluate the convergence behavior of the trace estimation, which is exact for d and D Hutchinson samples in latent and data space respectively, we compute the relative gradient distance of the resulting

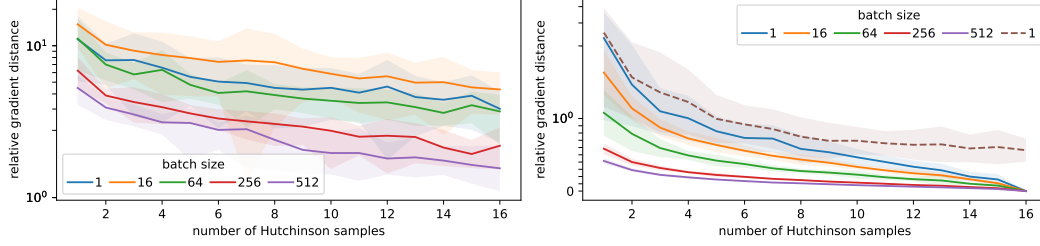


Figure 5: Relative gradient distance to the exact surrogate gradient as a function of Hutchinson samples for varying batch sizes. (Left) Trace estimation in data space. (Right) Trace estimation in latent space. We estimate the trace using orthogonalized Gaussian noise (see appendix D.3.5) (solid lines), but also feature non-orthogonalized samples for batch size 1 in latent space (dashed line). Note the different scales on the y-axes and the use of `symlog` in the right-hand plot. We evaluate the trace estimation on the surrogate estimator with gradient to encoder as specified in table 3 for a converged model trained on conditional MNIST ($d = 16$, $D = 784$).

surrogate gradient with respect to the exact solution as a function of Hutchinson samples K :

$$\text{relative gradient distance}(K) = \frac{\|\nabla \text{surrogate}(K) - \nabla \text{exact}\|_2}{\|\nabla \text{exact}\|_2}. \quad (89)$$

Here, $\nabla \text{surrogate}(K)$ denotes the gradient of the surrogate loss term after K Hutchinson samples and ∇exact the gradient of the exact surrogate loss term, i.e. after d or D samples.

In fig. 5 one can see a clear decrease in gradient distance and its variance when computing the trace in latent space instead of data space. Furthermore, we note that increasing the batch size also contributes to fast and steady convergence, which is a result of sampling an independent noise sample per batch instance.

D.2 Forward/backward automatic differentiation

Two of the basic building blocks of automatic differentiation (autodiff) libraries are the vector-Jacobian product (`vjp`) and the Jacobian-vector product (`jvp`). The `vjp` is implemented by backward-mode autodiff and computes a vector multiplied with a Jacobian matrix from the left, along with the output of the function being used:

$$f(x), \epsilon^\top f'(x) = \text{vjp}(f, x, \epsilon) \quad (90)$$

In PyTorch, this is implemented by the `torch.autograd.functional.vjp` function, or by first computing $f(x)$, then using `torch.autograd.grad`.

The `jvp` is implemented by forward-mode autodiff and computes a vector multiplied by a Jacobian matrix from the right, along with the output of the function being used:

$$f(x), f'(x)\epsilon = \text{jvp}(f, x, \epsilon) \quad (91)$$

In PyTorch, this is implemented by the `torch.autograd.forward_ad` package.

Our preferred estimator for the log-determinant is the following (see section 4.2):

$$-\frac{1}{K} \sum_{k=1}^K \epsilon_k^\top f'(x) \text{stop_gradient}(g'(z)\epsilon_k) \quad (92)$$

Therefore we need to compute terms of the form $\epsilon^\top f'(x)g'(z)\epsilon$, with a `stop_gradient` operation. The `stop_gradient` operation is implemented by applying the `.detach()` method to a tensor in PyTorch. We have the following options. Note that we can use a product obtained from `vjp` or `jvp` as a vector input to a subsequent product.

Backward mode This mode uses only vector-Jacobian products, requiring backward-mode autodiff.

1. $v_1^\top = \epsilon^\top f'(x)$ $z, v_1^\top = \text{vjp}(f, x, \epsilon)$
2. $v_2^\top = v_1^\top g'(z)$ $\hat{x}, v_2^\top = \text{vjp}(g, z, v_1)$
3. $\epsilon^\top f'(x)g'(z)\epsilon = v_2^\top \epsilon$

Forward mode This mode uses only Jacobian-vector products, requiring forward-mode autodiff.

1. $v_1 = g'(z)\epsilon$ $\hat{x}, v_1 = \text{jvp}(g, z, \epsilon)$
2. $v_2 = f'(x)v_1$ $z, v_2 = \text{jvp}(f, x, v_1)$
3. $\epsilon^\top f'(x)g'(z)\epsilon = \epsilon^\top v_2$

Mixed mode This mode uses one vector-Jacobian and one Jacobian-vector product, requiring both forward- and backward-mode autodiff.

1. $v_1^\top = \epsilon^\top f'(x)$ $z, v_1 = \text{vjp}(f, x, \epsilon)$
2. $v_2 = g'(z)\epsilon$ $\hat{x}, v_2 = \text{jvp}(g, z, \epsilon)$
3. $\epsilon^\top f'(x)g'(z)\epsilon = v_1^\top v_2$

We prefer using backward mode autodiff where possible, since we find that it is slightly faster than forward mode in PyTorch. However for our estimator of choice, we use mixed mode, since this is most easily implemented. Using backward mode would require a `stop_gradient` operation to be introduced after the second step, but in a way that allows gradient to flow back to $f'(x)$. While we believe this is possible if implemented carefully, we did not pursue this option. In mixed mode, we can easily detach the gradient of v_2 without affecting the first step of the calculation.

D.3 Properties of trace estimator noise

Hutchinson style trace estimators [Hutchinson, 1989] have the form $E_\epsilon[\epsilon^\top A \epsilon]$ and equal $\text{tr}(A)$ in expectation. If A is skew-symmetric ($A^\top = -A$), then $(\epsilon^\top A \epsilon)^\top = \epsilon^\top A^\top \epsilon = -\epsilon^\top A \epsilon$ and hence $\epsilon^\top A \epsilon = 0$ with zero variance. Since any matrix can be decomposed into a symmetric and skew-symmetric part, the variance in the estimator comes only from the symmetric part of A , namely $A_s = (A + A^\top)/2$. From now on, suppose A is symmetric and if not, substitute A_s for A .

D.3.1 Rademacher noise

If the entries of ϵ are sampled independently from a distribution with zero mean and unit variance, then the variance of the estimator is minimized by the Rademacher distribution which samples the values -1 and 1 each with probability half. This estimator achieves the following variance for symmetric A (see proposition 1 in Hutchinson [1989]):

$$V_\epsilon[\epsilon^\top A \epsilon] = 2 \sum_{i \neq j} A_{ij}^2 \quad (93)$$

D.3.2 Gaussian noise

With standard normal noise, the estimator is unbiased, but the variance is higher (see again Hutchinson [1989]):

$$V_\epsilon[\epsilon^\top A \epsilon] = 2 \sum_{i,j} A_{ij}^2 = 2\|A\|_F^2 \quad (94)$$

i.e. twice the Frobenius norm.

D.3.3 Scaled Gaussian noise

By contrast

$$E_\epsilon \left[\frac{\epsilon^\top A \epsilon}{\epsilon^\top \epsilon} \right] = \frac{1}{d} \text{tr}(A) \quad (95)$$

where ϵ is a standard normal variable in \mathbb{R}^d . The variance of this estimator for symmetric A (see theorem 2.2 in Girard [1989]) is:

$$V_\epsilon \left[\frac{\epsilon^\top A \epsilon}{\epsilon^\top \epsilon} \right] = \frac{2}{d+2} \sigma^2(\lambda(A)) \quad (96)$$

where $\sigma^2(\lambda(A))$ denotes the variance of the eigenvalues of A .

We can write this estimator in the ‘‘Hutchinson’’ form by sampling ϵ from a standard normal distribution, then normalizing it such that its length is \sqrt{d} . Then we have

$$E_\epsilon[\epsilon^\top A \epsilon] = \text{tr}(A) \quad (97)$$

and

$$V_\epsilon[\epsilon^\top A \epsilon] = \frac{2d^2}{d+2} \sigma^2(\lambda(A)) \quad (98)$$

D.3.4 Comparison

When the dimension of A becomes large, the variance of Rademacher and scaled Gaussian estimators are comparable. Suppose that the eigenvalues of A have zero mean (e.g. the entries are independent normal samples). Then

$$d\sigma^2(\lambda(A)) = \sum_i \lambda_i^2 = \text{tr}(A^2) = \|A\|_F^2 \quad (99)$$

If we further assume that all entries of A have roughly equal magnitude we have that

$$\sum_{i \neq j} A_{ij}^2 \approx \|A\|_F^2 \quad (100)$$

since the sum in the Frobenius norm is dominated by the $d(d-1)$ off-diagonal terms. Similarly,

$$\frac{d^2}{d+2} \sigma^2(\lambda(A)) \approx d\sigma^2(\lambda(A)) = \|A\|_F^2 \quad (101)$$

meaning that the two estimators have approximately the same variance.

If the matrix has special structure, we might choose one estimator over the other. For example, if the standard deviation of the eigenvalues of A is small in comparison to the mean eigenvalue, the scaled Gaussian estimator is preferable and if A is dominated by its diagonal then the Rademacher estimator is preferable. We don’t expect either type of special structure in our matrices, so we consider the estimators interchangeable. We decided to use scaled Gaussian noise since it produces noise which points in all possible directions in \mathbb{R}^d whereas Rademacher noise is restricted to a finite 2^d points. We assume that there is no reason to prefer this set of 2^d directions and therefore sampling from all possible directions is better.

D.3.5 Reducing variance when sampling more than 1 Hutchinson sample

When the number of Hutchinson samples K are greater than 1, it is more favorable to sample the noise vectors in a dependent way than independently. Consider the case of a $d \times d$ matrix A with $K = d$. Then we can get an exact estimate of the trace via

$$\sum_{i=1}^d q_i^\top A q_i = \text{tr}(Q^\top A Q) = \text{tr}(A) \quad (102)$$

with orthogonal Q and q_i the i -th column of Q . If the q_i were sampled independently, we almost certainly wouldn’t achieve this exact result. We therefore sample our noise vectors as the first K columns of a randomly sampled $d \times d$ orthogonal matrix and scale each column by \sqrt{d} . We show below that this reduces variance compared with sampling independently and make an experimental comparison (see fig. 5). If the resulting noise vectors are denoted ϵ_i , we estimate $\text{tr}(A)$ by

$$\widehat{\text{tr}}(A) = \frac{1}{K} \sum_{i=1}^K \epsilon_i^\top A \epsilon_i \quad (103)$$

This estimator is unbiased:

$$E_{\epsilon_1, \dots, \epsilon_K}[\widehat{\text{tr}}(A)] = \frac{1}{K} \sum_{i=1}^K E_{\epsilon_i}[\epsilon_i^\top A \epsilon_i] \quad (104)$$

$$= \frac{1}{K} \sum_{i=1}^K \text{tr}(A E_{\epsilon_i}[\epsilon_i \epsilon_i^\top]) \quad (105)$$

$$= \frac{1}{K} \sum_{i=1}^K \text{tr}(A) \quad (106)$$

$$= \text{tr}(A) \quad (107)$$

since $E_{\epsilon_i}[\epsilon_i \epsilon_i^\top] = \mathbb{I}$ for all ϵ_i .

This procedure is equivalent to using scaled Gaussian noise when $K = 1$ and is what we implement in practice for all values of K . Note that it is not necessary to use $K > d$ since we already achieve the exact value with $K = d$.

A note on our sampling strategy: in practice we sample by taking the Q matrix of the QR decomposition of a $d \times K$ matrix with entries sampled from a standard normal. Since the QR decomposition performs Gram-Schmidt orthogonalization, the Q matrix is uniformly sampled from the group of orthogonal matrices if Q is square [Mezzadri, 2006]. The same logic applies to the QR decomposition of non-square matrices, yielding a $d \times K$ matrix made up of the first K columns of a uniformly sampled orthogonal $d \times d$ matrix. Strictly speaking, the QR decomposition is only unique if the R matrix has a positive diagonal, and uniqueness is required for uniform sampling. Let $X = QR$ and define by D the sign of the diagonal of R . D is diagonal with 1 or -1 on the diagonal and $D^2 = \mathbb{I}$. Uniqueness can be achieved by multiplying Q by D from the right and multiplying R by D from the left: $X = QDDR = QR$. The resulting uniformly sampled orthogonal matrix is QD , meaning the columns of Q are multiplied by either 1 or -1 . In our setting, we have terms of the form $\epsilon_i^\top A \epsilon_i$ where the ϵ_i are the columns of Q , so multiplying the columns by -1 has no effect on the trace estimate. As a result we opt not to multiply by D . Therefore, although we do not sample uniformly from the orthogonal group, the final result is equivalent to sampling uniformly.

Variance derivation Using the formula for the variance of a sum of random variables, we have that

$$V_{\epsilon_1, \dots, \epsilon_K}[\widehat{\text{tr}}(A)] = \frac{1}{K^2} \sum_{i,j=1}^K C_{\epsilon_i, \epsilon_j}[\epsilon_i^\top A \epsilon_i, \epsilon_j^\top A \epsilon_j] \quad (108)$$

where C denotes the covariance between two random variables. Note that since the permutation of the columns of a randomly sampled orthogonal matrix is arbitrary (permuting the columns results in another randomly sampled orthogonal matrix of equal probability), all columns are equivalent and we only have to distinguish between the cases $i = j$ and $i \neq j$. This leads to²

$$V_{\epsilon_1, \dots, \epsilon_K}[\widehat{\text{tr}}(A)] = \frac{1}{K^2} (Kv + K(K-1)c) = \frac{1}{K} (v + (K-1)c) \quad (109)$$

with $v = V_{\epsilon_i}[\epsilon_i^\top A \epsilon_i]$ and $c = C_{\epsilon_i, \epsilon_j}[\epsilon_i^\top A \epsilon_i, \epsilon_j^\top A \epsilon_j]$ when $i \neq j$. Each column viewed individually is a randomly sampled Gaussian vector, scaled to have length \sqrt{d} , hence the value of v is equal to the scaled Gaussian noise case above, namely

$$v = \frac{2d^2}{d+2} \sigma^2(\lambda(A)) \quad (110)$$

where $\sigma^2(\lambda(A))$ denotes the variance of the eigenvalues of A . We also know that the variance of the estimator reduces to zero when $K = d$ and hence $v + (d-1)c = 0$ leading to

$$c = -\frac{v}{d-1} \quad (111)$$

²This argument is inspired by <https://math.stackexchange.com/questions/1081345/finding-variance-of-the-sample-mean-of-a-random-sample-of-size-n-without-replace>

Putting it all together leads to

$$V_{\epsilon_1, \dots, \epsilon_K}[\widehat{\text{tr}}(A)] = \frac{1}{K} \left(v - \frac{K-1}{d-1} v \right) \quad (112)$$

$$= \frac{1}{K} \frac{d-K}{d-1} v \quad (113)$$

$$= \frac{2d^2(d-K)}{K(d-1)(d+2)} \sigma^2(\lambda(A)) \quad (114)$$

valid for $d > 1$. The comparable quantity for independently sampled scaled Gaussian noise is

$$V_{\epsilon_1, \dots, \epsilon_K}[\widehat{\text{tr}}(A)] = \frac{2d^2}{K(d+2)} \sigma^2(\lambda(A)) \quad (115)$$

i.e. $1/K$ times the $K = 1$ result. The orthogonalized noise strategy always has lower variance since the ratio between the variances is

$$\frac{d-K}{d-1} \leq 1 \quad (116)$$

which even reduces to zero when $K = d$. If d is large, the difference is not great for small K , which aligns with the fact that randomly sampled directions in \mathbb{R}^d are close to orthogonal for large d .

E Experimental Details

E.1 Toy data

To analyze the model behaviour depending on the reconstruction weight β , we train the same architecture on a simple sinusoid data set with β varied between 0.01 and 100.

For the generation of data points, we draw x positions from a 1D standard normal distribution and calculate the respective y positions by $y = \sin(\pi x/2)$. Then, isotropic Gaussian noise with $\sigma = 0.1$ is added. We train an autoencoder architecture built with four residual blocks and a 1D latent space for 50 epochs with learning rate 0.001 until convergence. Each residual block is made up of a feedforward network with one hidden layer of width 256. For each β , 20 models are trained.

To visualize the dimension of the data that is captured by the model, we project samples from the data distribution to the (1D) latent space and color the data points using the respective latent code as color value. Figure 3 illustrates that low reconstruction weight β values result in learning the dimension with the lowest entropy (noise) and higher values are required to learn the manifold that spans the sinusoid.

Additionally, we repeat the procedure with higher noise levels ($\sigma = 0.2, 0.3$). We observe that the point at which the model transitions from learning the noise to representing the manifold is not fixed, but depends on features of the data set such as the noise (fig. 6).

E.2 Conditional MNIST

Depending on the reconstruction weight β in eq. (8), we want to evaluate how much structure of the original dataset can be reproduced by the generating (decoding) model g . For a given latent space input, we compute the full decoder Jacobian matrix J by calculating d Jacobian-vector products (one per column of the Jacobian). We compute the singular values $\Sigma = \text{diag}(s_1, \dots, s_d)$ of J , which – roughly speaking – indicate the stretching or shrinking of the latent manifold by g . Hence, the number of non-vanishing singular values suggest the dimension of the data manifold and the sum of the log singular values is equal to the change in entropy between the latent space and data space, where a higher entropy indicates that more of the data manifold is spanned by the decoder. We can see this from the formula

$$H(p_X) = H(p_Z) + E_{p_Z} \left[\frac{1}{2} \log \det(g'(z)^\top g'(z)) \right] \quad (117)$$

with H the differential entropy, and noting that $2 \text{tr} \log \Sigma = \log \det(g'(z)^\top g'(z))$.

We train multiple MLAEs on conditional MNIST with reconstruction weights β ranging from 0.1 to 100, and evaluate their singular value spectra. The models are trained for 400 epochs, which is

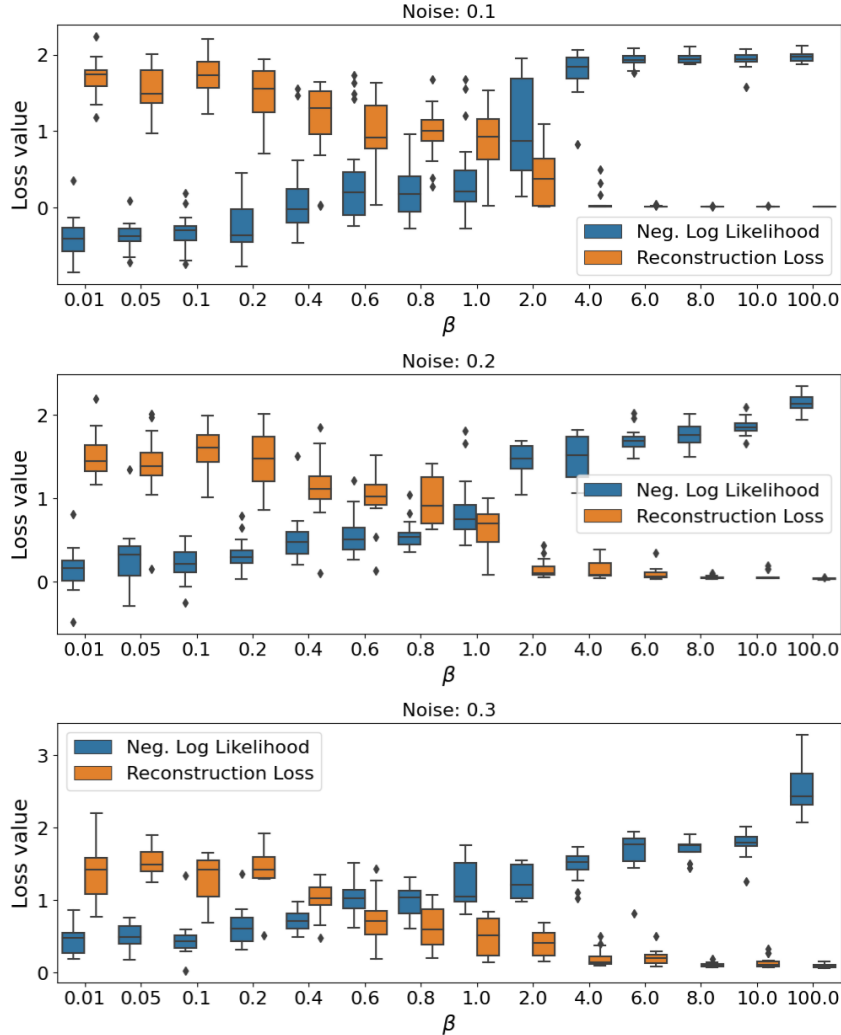


Figure 6: The position of the transition point depends on the data set. The plots show the tradeoff between reconstruction error and NLL with reconstruction weight β (box plots summarize 20 runs per condition). The point at which β becomes sufficiently large (transition point) shifts to lower values with increased Gaussian noise added to the data points.

sufficient for convergence. The architecture used is the same as in table 9, except that it has four times as many channels in each convolutional layer.

In fig. 7 it is clear that a higher reconstruction weight gives rise to a higher number of non-vanishing singular values. Hence, the reconstruction weight contributes towards learning structure of the true data manifold. This observed additional structure for higher reconstruction weights is reflected in an increasing diversity of samples (see fig. 8). Nevertheless, for high reconstruction weights we note the trade-off between sample diversity and properly learned latent distributions, which might result in out of distribution samples.

E.3 Tabular data

We compare to the tabular data experiments in Caterini et al. [2021], using the same datasets and data splits, as well as the same latent space dimensions. We train models with roughly the same number of parameters. Our main architectural difference is that we use an unconstrained autoencoder rather than an injective flow. Our encoder consists of two parts: i) a feed-forward network with two hidden layers of dimension 256 and ReLU activations (no normalization layers), which maps from

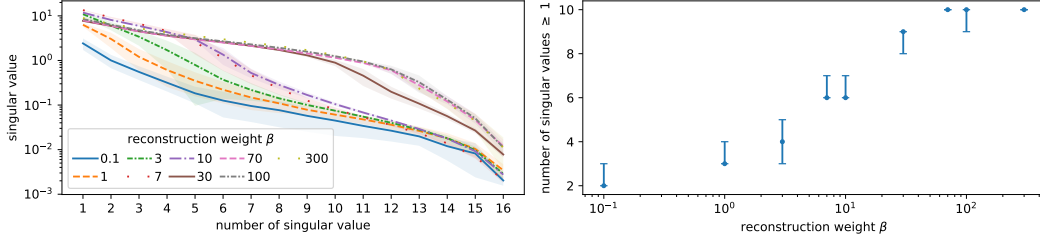


Figure 7: (Left) Singular value spectra for varying reconstruction weight. (Right) Number of singular values greater or equal to one as a function of reconstruction weight. The error bars show the span of the intersection of the shaded region with the line $y = 1$ in the left hand plot, rounded down to the nearest integer. For each trained model we generate 1024 samples per condition, compute the singular value spectra and average over all samples regardless of condition. The mean spectra and their standard deviation are evaluated across five trained models per reconstruction weight.

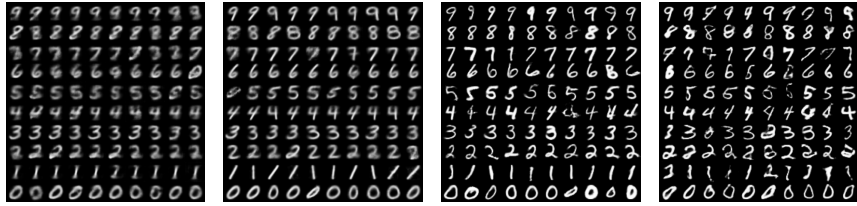


Figure 8: Conditional MNIST samples for varying reconstruction weight β . For each value of $\beta \in [0.1, 1, 10, 100]$ (from left to right), and each condition (rows) we generate ten samples (columns) at temperature $T = 1$.

the input dimension to the latent dimension ii) a ResNet with two blocks, each with two hidden layers of dimension 256 and ReLU activations. The ResNet has input and output dimension equal to the latent space dimension. The decoder is the inverse: i) an identical ResNet to the encoder (but with separate parameters) followed by ii) a feed-forward network with two hidden layers of dimension 256 mapping from the latent space to the data space dimension.

We use a batch size of 512, add isotropic Gaussian noise with standard deviation 0.01, use $K = 1$ Hutchinson samples and a reconstruction weight $\beta = 10$ for all experiments. We use the Adam optimizer with the onecycle LR scheduler with LR of 3×10^{-4} and weight decay of 10^{-4} . The number of epochs was chosen such that all experiments had approximately the same number of training iterations. We ran the model 5 times per dataset. The dataset-dependent parameters and average runtimes are given in table 4.

We compare our runtimes against the published rectangular flow runtimes for their RNFs-ML ($K = 1$) model, as well as rerunning their code on our hardware (a single RTX 2070 card). We find comparable FID-like scores on our rerun, but our hardware is slower, with runs consistently taking at least 15% longer and more than twice as long on MINIBOONE. We find that our model runs in 1/10th the time or less of the rectangular flow on the same hardware, except for MINIBOONE (about 1/8th the time).

E.4 Image datasets

Pythae benchmark We compare our method to existing generative autoencoder paradigms using the benchmark from Chadebec et al. [2022]. We use the provided open-source pipeline and follow the training setup described by the authors. For MNIST and CIFAR10 this means training for 100 epochs with the Adam optimizer at a starting LR of 10^{-4} , reserving the last 10k images of the training sets as validation sets. CelebA trains for 50 epochs with a starting LR of 10^{-3} . All experiments are performed with a batch size of 100 and LR is reduced by half when the loss plateaus for 10 epochs. In accordance with the original benchmark we pick 10 sets of hyper-parameters, compute their validation FID (see fig. 9) and use the model which achieves the best FID on the validation set as the final model. In table 5 we report the FID and IS of this model on the test set. Not only does our method produce realistic samples as indicated by the low FID (see fig. 10), but we also consistently

Table 4: Dataset-dependent hyperparameters and average total runtime for tabular data experiments. We compare our runtime against the published rectangular flow [Caterini et al., 2021] runtimes (RNFs-ML ($K = 1$) model), as well as rerunning their code on our hardware.

Hyperparameter	POWER	GAS	HEPMASS	MINIBOONE
Latent dimension	3	2	10	21
Training epochs	3	6	17	170
Runtime (minutes)				
MLAE (<i>ours</i>)	7.6	7.8	8.2	9.8
Rectangular flow (published)	113	75	138	34
Rectangular flow (our hardware)	147	86	249	75

achieve an IS at the high end of the benchmark. This translates to the large variability in samples seen in our experiments.

As described in section 5.2, we use the architectures from Chadebec et al. [2022] for the benchmark, which we replicate in tables 7 and 8.

Best-performing models The potential of maximum likelihood autoencoders (MLAE) is not yet exploited by the Pythae benchmark. To demonstrate this, we identify the best performing model for MNIST and CelebA trained during method development, whose samples are shown in fig. 1.

The identified models differ in the following from Pythae: (a) In addition to the mainly convolutional architecture for encoder and decoder in Pythae, the models have more subsequent fully-connected layers with skip connections, see table 9. (b) We train longer, for 2000 epochs on MNIST and 200 on CelebA (Pythae trains for 100 respectively 50 epochs). (c) We increase the batch size to 512 (MNIST) respectively 256 (CelebA). On MNIST only: (d1) we linearly increase the reconstruction weight $\beta(\text{epoch})$ as a function of the epoch, from a factor 1 (at epoch=0) up to 10 (at epoch=max_epoch), (d2) we regularize the parameters with a weight decay of 10^{-4} , and (d3) we do not make use of BatchNorm, as our gradient estimator does not allow for within-batch dependencies.

Ablation To judge the importance of these changes, we perform an ablation where we successively modify the best models on MNIST and CelebA.

We report the variants tried and the resulting FID scores in table 6, and show samples of the best models in the ablation in fig. 11. We mainly observe that training with our improved architecture “ConvNet+” (a) yields significantly better performance than training with the standard architecture on both MNIST and CelebA. The difference in performance between the normal sampler and the GMM sampler shrinks, indicating that this architecture is better suited to shape the latent space to a normal distribution, and that there is training signal from our MLAE loss for the latent distribution to become more Gaussian.

The influence of the architecture is stronger than the influence of other training hyperparameters, of which we try several different combinations (see table 6). All models in the ablation are trained with more epochs (b) and larger batches (c).

We conclude that the Pythae benchmark could benefit from an optimized architecture, as this change probably also improves the other methods. From the data at hand, we further conclude that the full potential of MLAE has not yet been exploited, and that easy gains can be made by improving the architecture and other hyperparameters.

E.5 Compute and dependencies

We used approximately 150 GPU hours for computing the Pythae benchmark, and an additional 800 GPU hours for model exploration and testing. The majority of the experiments were performed on an internal cluster of A100s. The majority of compute time was spent on image datasets.

We build our code upon the following python libraries: PyTorch [Paszke et al., 2019], PyTorch Lightning [Falcon and The PyTorch Lightning team, 2019], Tensorflow [Abadi et al., 2015] for FID

score evaluation, Numpy [Harris et al., 2020], Matplotlib [Hunter, 2007] for plotting and Pandas [Wes McKinney, 2010, pandas development team, 2020] for data evaluation.

Table 5: Table taken from Chadebec et al. [2022] with our results added at the top. We report Inception Score (IS) and Fréchet Inception Distance (FID) computed with 10k samples on the test set. The best model per dataset and sampler is highlighted in **bold**, the second best is underlined.

Model	Sampler	MNIST		ConvNet CIFAR10		CELEBA		MNIST		ResNet CIFAR10		CELEBA	
		FID ↓	IS ↑	FID	IS	FID	IS ↑	FID ↓	IS ↑	FID	IS	FID	IS
MLAE (ours)	\mathcal{N}	23.8	2.2	121.0	3.0	56.9	2.1	19.5	2.1	132.6	2.9	62.3	1.7
	GMM	11.0	2.2	90.6	4.0	<u>47.3</u>	1.9	11.7	2.1	119.2	3.4	55.0	1.8
VAE	\mathcal{N}	28.5	2.1	241.0	2.2	54.8	1.9	31.3	2.0	181.7	2.5	66.6	1.6
	GMM	26.9	2.1	235.9	2.3	52.4	1.9	32.3	2.1	179.7	2.5	63.0	1.7
VAMP	VAMP	64.2	2.0	329.0	1.5	56.0	1.9	34.5	2.1	181.9	2.5	67.2	1.6
IWAE	\mathcal{N}	29.0	2.1	245.3	2.1	55.7	1.9	32.4	2.0	191.2	2.4	67.6	1.6
	GMM	28.4	2.1	241.2	2.1	52.7	1.9	34.4	2.1	188.8	2.4	64.1	1.7
VAE-lin NF	\mathcal{N}	29.3	2.1	240.3	2.1	56.5	1.9	32.5	2.0	185.5	2.4	67.1	1.6
	GMM	28.4	2.1	237.0	2.2	53.3	1.9	33.1	2.1	183.1	2.5	62.8	1.7
VAE-IAF	\mathcal{N}	27.5	2.1	236.0	2.2	55.4	1.9	30.6	2.0	183.6	2.5	66.2	1.6
	GMM	27.0	2.1	235.4	2.2	53.6	1.9	32.2	2.1	180.8	2.5	62.7	1.7
β -VAE	\mathcal{N}	21.4	2.1	115.4	3.6	56.1	1.9	19.1	2.0	124.9	3.4	65.9	1.6
	GMM	9.2	2.2	92.2	3.9	51.7	1.9	11.4	2.1	<u>112.6</u>	3.6	59.3	1.7
β -TC VAE	\mathcal{N}	21.3	2.1	116.6	2.8	55.7	1.8	20.7	2.0	125.8	3.4	65.9	1.6
	GMM	11.6	2.2	<u>89.3</u>	4.1	51.8	1.9	13.3	2.1	106.5	3.7	59.3	1.7
FactorVAE	\mathcal{N}	27.0	2.1	236.5	2.2	53.8	1.9	31.0	2.0	185.4	2.5	66.4	1.7
	GMM	26.9	2.1	234.0	2.2	52.4	2.0	32.7	2.1	184.4	2.5	63.3	1.7
InfoVAE - RBF	\mathcal{N}	27.5	2.1	235.2	2.1	55.5	1.9	31.1	2.0	182.8	2.5	66.5	1.6
	GMM	26.7	2.1	230.4	2.2	52.7	1.9	32.3	2.1	179.5	2.5	62.8	1.7
InfoVAE - IMQ	\mathcal{N}	28.3	2.1	233.8	2.2	56.7	1.9	31.0	2.0	182.4	2.5	66.4	1.6
	GMM	27.7	2.1	231.9	2.2	53.7	1.9	32.8	2.1	180.7	2.6	62.3	1.7
AAE	\mathcal{N}	<u>16.8</u>	2.2	139.9	2.6	59.9	1.8	19.1	2.1	164.9	2.4	64.8	1.7
	GMM	9.3	2.2	92.1	3.8	53.9	2.0	11.1	2.1	118.5	3.5	58.7	1.8
MSSSIM-VAE	\mathcal{N}	26.7	2.2	279.9	1.7	124.3	1.3	28.0	2.1	254.2	1.7	119.0	1.3
	GMM	27.2	2.2	279.7	1.7	124.3	1.3	28.8	2.1	253.1	1.7	119.2	1.3
VAEGAN	\mathcal{N}	8.7	2.2	199.5	2.2	39.7	1.9	12.8	2.2	198.7	2.2	122.8	2.0
	GMM	6.3	2.2	197.5	2.1	35.6	1.8	6.5	2.2	188.2	2.6	84.3	1.7
AE	\mathcal{N}	26.7	2.1	201.3	2.1	327.7	1.0	221.8	1.3	210.1	2.1	275.0	2.9
	GMM	9.3	2.2	97.3	3.6	55.4	2.0	11.0	2.1	120.7	3.4	57.4	1.8
WAE - RBF	\mathcal{N}	21.2	2.2	175.1	2.0	332.6	1.0	21.2	2.1	170.2	2.3	69.4	1.6
	GMM	9.2	2.2	97.1	3.6	55.0	2.0	11.2	2.1	120.3	3.4	58.3	1.7
WAE - IMQ	\mathcal{N}	18.9	2.2	164.4	2.2	64.6	1.7	20.3	2.1	150.7	2.5	67.1	1.6
	GMM	8.6	2.2	96.5	3.6	51.7	2.0	11.2	2.1	119.0	3.5	57.7	1.8
VQVAE	\mathcal{N}	28.2	2.0	152.2	2.0	306.9	1.0	170.7	1.6	195.7	1.9	140.3	2.2
	GMM	9.1	2.2	95.2	3.7	51.6	2.0	<u>10.7</u>	2.1	120.1	3.4	57.9	1.8
RAE-L2	\mathcal{N}	25.0	2.0	156.1	2.6	86.1	2.8	63.3	2.2	170.9	2.2	168.7	3.1
	GMM	9.1	2.2	85.3	3.9	55.2	1.9	11.5	2.1	122.5	3.4	58.3	1.8
RAE - GP	\mathcal{N}	27.1	2.1	196.8	2.1	86.1	2.4	61.5	2.2	229.1	2.0	201.9	3.1
	GMM	9.7	2.2	96.3	3.7	52.5	1.9	11.4	2.1	123.3	3.4	59.0	1.8

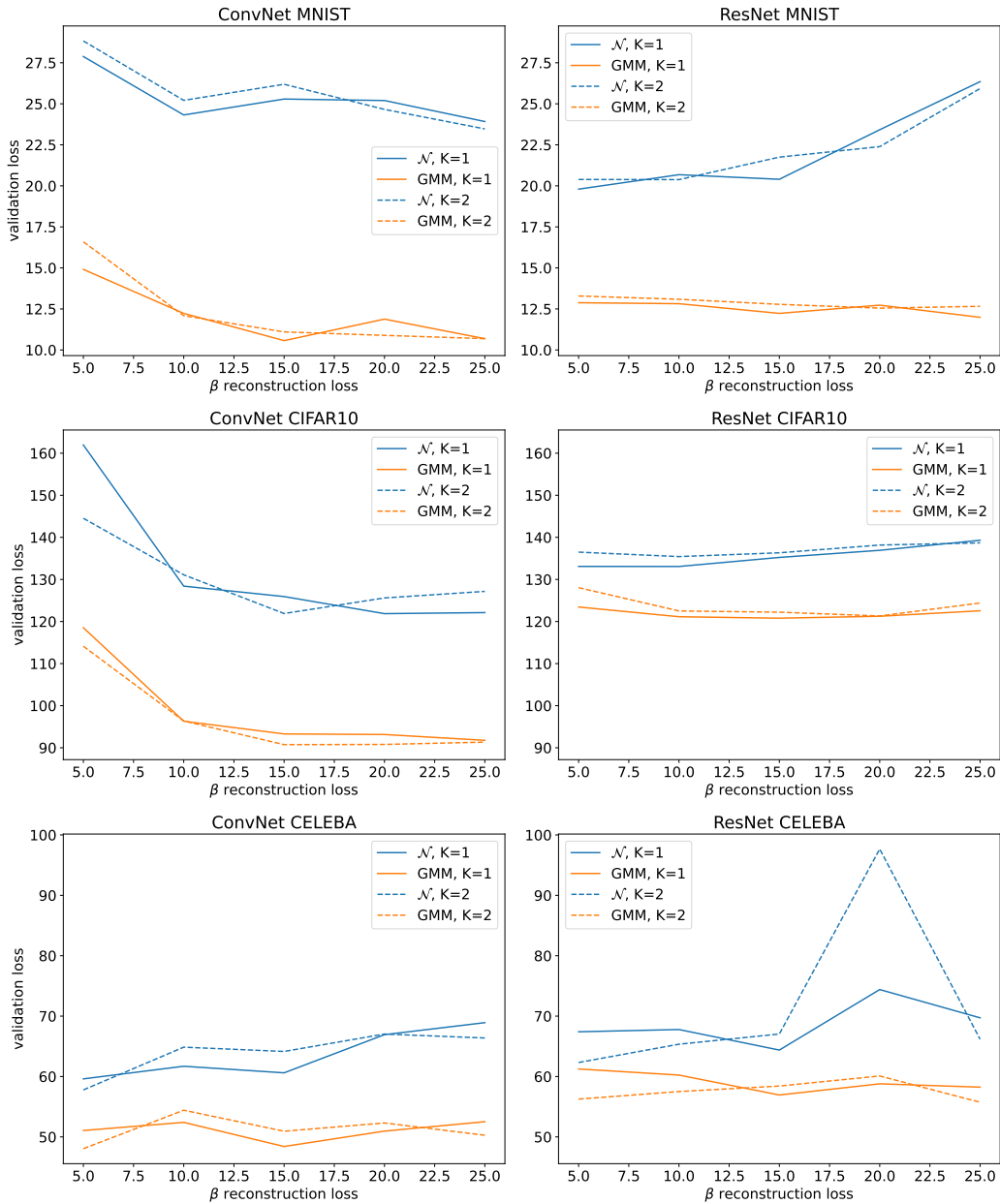


Figure 9: Validation FID of our 10 benchmark model setups on the different datasets and architectures used by Pythae. We report results for reconstruction weights $\beta = 5, 10, 15, 20, 25$ and number of Hutchinson samples $K = 1$ in the solid lines and $K = 2$ in the dashed lines. We show the performance of standard normal sampling (\mathcal{N}) and a Gaussian mixture model (GMM). We see that GMM sampling always improves performance. In contrast, the reconstruction weight and number of Hutchinson samples have no noticeable effect on performance, except that increasing β improves performance on ConvNet MNIST and ConvNet CIFAR10, and decreases performance on ResNet MNIST (normal sampling only).

Table 6: **Ablation study on training and architecture choice.** Δ FID (lower is better) denotes the difference between FID scores with normal sampler and GMM sampler. A score of Δ FID = 0 would indicate that fitting a GMM to the latent space does not improve the sample quality. Most importantly, the architecture with additional fully connected layers (ConvNet+) greatly improve the performance for the normal sampler, although the number of parameters is decreased or kept roughly constant, see table 9. BN denotes the variant with BatchNorm, β (epoch) denotes the variant with increasing reconstruction weight, and weight decay indicates training with weight decay.

Architecture	MNIST			CelebA		
	FID \mathcal{N}	FID GMM	Δ FID	FID \mathcal{N}	FID GMM	Δ FID
ConvNet+, β (epoch), weight decay	11.5	9.3	2.2	-	-	-
ConvNet+, weight decay	11.3	9.1	2.2	48.7	40.9	7.9
ConvNet+, BN	16.8	13.3	3.5	47.7	36.5	11.1
ConvNet+	14.3	10.1	4.2	51.1	41.4	9.7
ConvNet	20.9	10.0	10.9	62.2	41.4	20.8
ConvNet, BN	24.6	13.8	10.8	54.3	36.8	17.5
ConvNet, weight decay	-	-	-	58.2	42.0	16.2
ConvNet, β (epoch)	23.1	9.9	13.3	-	-	-

Table 7: **ConvNet**, neural network architecture used for the convolutional networks, adapted from Chadebec et al. [2022].

	MNIST	CIFAR10	CELEBA
Encoder	(1, 28, 28)	(3, 32, 32)	(3, 64, 64)
Layer 1	Conv(128, 4, 2), BN, ReLU	Conv(128, 4, 2), BN, ReLU	Conv(128, 4, 2), BN, ReLU
Layer 2	Conv(256, 4, 2), BN, ReLU	Conv(256, 4, 2), BN, ReLU	Conv(256, 4, 2), BN, ReLU
Layer 3	Conv(512, 4, 2), BN, ReLU	Conv(512, 4, 2), BN, ReLU	Conv(512, 4, 2), BN, ReLU
Layer 4	Conv(1024, 4, 2), BN, ReLU	Conv(1024, 4, 2), BN, ReLU	Conv(1024, 4, 2), BN, ReLU
Layer 5	Linear(1024, latent_dim)*	Linear(4096, latent_dim)*	Linear(16384, latent_dim)*
Decoder			
Layer 1	Linear(latent_dim, 16384)	Linear(latent_dim, 65536)	Linear(latent_dim, 65536)
Layer 2	ConvT(512, 3, 2), BN, ReLU	ConvT(512, 4, 2), BN, ReLU	ConvT(512, 5, 2), BN, ReLU
Layer 3	ConvT(256, 3, 2), BN, ReLU	ConvT(256, 4, 2), BN, ReLU	ConvT(256, 5, 2), BN, ReLU
Layer 4	Conv(1, 3, 2), Sigmoid	Conv(3, 4, 1), Sigmoid	ConvT(128, 5, 2), BN, ReLU
Layer 5	-	-	ConvT(3, 5, 1), Sigmoid
#Parameters	17.2M	39.4M	33.5M

Table 8: **ResNet**, neural network architecture used for the residual networks, adapted from Chadebec et al. [2022].

	MNIST	CIFAR10	CELEBA
Encoder	(1, 28, 28)	(3, 32, 32)	(3, 64, 64)
Layer 1	Conv(64, 4, 2)	Conv(64, 4, 2)	Conv(64, 4, 2)
Layer 2	Conv(128, 4, 2)	Conv(128, 4, 2)	Conv(128, 4, 2)
Layer 3	Conv(128, 3, 2)	Conv(128, 3, 1)	Conv(128, 3, 2)
Layer 4	ResBlock*	ResBlock*	Conv(128, 3, 2)
Layer 5	ResBlock*	ResBlock*	ResBlock*
Layer 6	Linear(2048, latent_dim)*	Linear(8192, latent_dim)*	ResBlock*
Layer 7	-	-	Linear(2048, latent_dim)*
Decoder			
Layer 1	Linear(latent_dim, 2048)	Linear(latent_dim, 8192)	Linear(latent_dim, 2048)
Layer 2	ConvT(128, 3, 2)	ResBlock*	ConvT(128, 3, 2)
Layer 3	ResBlock*	ResBlock*	ResBlock*
Layer 4	ResBlock*, ReLU	ConvT(64, 4, 2)	ResBlock*
Layer 5	ConvT(64, 3, 2), ReLU	ConvT(3, 4, 2), Sigmoid	ConvT(128, 5, 2), Sigmoid
Layer 6	ConvT(1, 3, 2), Sigmoid	-	ConvT(64, 5, 2), Sigmoid
Layer 6	-	-	ConvT(3, 4, 2), Sigmoid
#Parameters	0.73M	4.7M	29.6M

*The ResBlocks are composed of one Conv(32, 3, 1) followed by Conv(128, 1, 1) with ReLU.

Table 9: **ConvNet+**, Neural network architecture used for the improved, changes from table 7 highlighted in *italic*. The relative change in number of parameters is computed in comparison to table 7.

	MNIST	CELEBA
Encoder	(1, 28, 28)	(3, 64, 64)
Layer 1	Conv(32, 4, 2), BN, ReLU	Conv(128, 4, 2), BN, ReLU
Layer 2	Conv(64, 4, 2), BN, ReLU	Conv(256, 4, 2), BN, ReLU
Layer 3	Conv(128, 4, 2), BN, ReLU	Conv(512, 4, 2), BN, ReLU
Layer 4	Conv(256, 4, 2), BN, ReLU	Conv(1024, 4, 2), BN, ReLU
Layer 5	Linear(256, latent_dim)*	Linear(16384, latent_dim)*
Layer 6-9	4xResBlock(512)	4xResBlock(256)
Decoder		
Layer 1-4	4xResBlock(512)	4xResBlock(256)
Layer 5	Linear(latent_dim, 4096)	Linear(latent_dim, 65536)
Layer 6	ConvT(256, 3, 2), BN, ReLU	ConvT(512, 5, 2), BN, ReLU
Layer 7	ConvT(128, 3, 2), BN, ReLU	ConvT(256, 5, 2), BN, ReLU
Layer 8	ConvT(64, 3, 2), BN, ReLU	ConvT(128, 5, 2), BN, ReLU
Layer 9	Conv(1, 3, 2), Sigmoid	ConvT(3, 5, 1), Sigmoid
#Parameters	3.3M (-81%)	34.3M (+2%)

*The ResBlocks(inner_dim) are composed of Linear(latent_dim, inner_dim), SiLU, Linear(inner_dim, inner_dim), SiLU, Linear(inner_dim, latent_dim) with a skip connection.



Figure 10: Uncurated samples of the models selected by the PythAE benchmark in table 5.



Figure 11: Uncurated samples of the best models in table 6, as determined by FID of samples from the normal sampler.